Methanol masers and millimetre lines : a common origin in protostellar envelopes

Torstensson, K.J.E.

CHAPTER 4

Distribution and excitation of thermal methanol in 6.7 GHz maser bearing star-forming regions

II. A sample of 14 sources

Abstract

The 6.7 GHz CH_3OH maser is exclusively associated with high-mass star formation and this signpost allows us to do statistical studies of high-mass star-forming regions. CH_3OH is thought to originate from the icy mantles of dust grains and released in shocks. Furthermore, CH_3OH excited in massive young stellar objects shows a rich spectrum. To understand the origin of the CH_3OH maser emission, we map the distribution and excitation of the thermal CH_3OH emission in a sample of 12 relatively nearby (<6 kpc) high-mass star forming regions that are identified through 6.7 GHz maser emission. JCMT observations of the $J = 7 \rightarrow 6$ band at 338 GHz are used to image the line emission of 25 transitions, with upper energy levels between 65 and 390 K, over a $2'$ field at $14''$ resolution. The images are velocity-resolved and allow us to study the kinematics of the regions. Further, rotation diagrams are created to derive rotation temperatures and column densities of the large scale molecular gas. The effects of optical depth and subthermal excitation are studied with population diagrams. For eight of the sources in our sample the thermal CH_3OH emission is confined to a region <0.4 pc and with a central peak close (<0.03 pc) to the position of the CH_3OH maser emission. Four sources have more extended thermal CH_3OH emission without a clear peak, and for the remaining two sources, the emission is too weak to map. The compact sources have linear velocity gradients along the semi-major axis of the emission of 0.3 – 13 km s^{-1} pc^{-1}. The rotation diagram analysis shows that in general the highest rotation temperature is found close to the maser position. The population diagram analysis of the gas at the maser position does not show signs of large beam dilution effects, but indicates moderate optical depths of the lower-K lines which reduces our estimate of the excitation temperature. The confined and centrally peaked CH_3OH emission in the compact sources indicates a single source for the CH_3OH gas

and the velocity fields show signs of outflow in all but one of the sources. The high detection rate of the torsionally excited $v_t = 1$ line and signs of high-K lines at the maser position indicate radiative pumping, though the general lack of measurable beam dilution effects may mean that the masing gas is not sampled well and originates in a very small region.

4.1 Introduction

In star-forming regions, maser action is commonly seen from various molecules (mostly OH, H_2O and CH_3OH ; sometimes NH_3; rarely SiO, H_2CO). Among these masers, the 6.7 GHz CH_3OH maser is unique because it is wide spread and exclusively associated with high-mass star formation (Minier et al. 2003, Xu et al. 2008). Much effort has gone into determining what physical component the maser emission traces (Norris et al. 1998, Pestalozzi et al. 2004, Minier et al. 2002, Bartkiewicz et al. 2005b). High resolution VLBI studies of the methanol masers indicate that they occur in physical structures on size scales of ∼1000 AU, close to the protostar(s) (Bartkiewicz et al. 2009). Other studies are focussing on determining whether the masers trace a mass range or a particular time range in the evolutionary sequence by observing the spectral energy distribution (SED) of the central objects (Breen et al. 2010, Pandian et al. 2009).

CH_3OH is a versatile probe of the physical conditions in these regions, since it is sensitive to both the temperature and density due to its slight asymmetry. However, care must be taken when choosing which transitions to observe as different bands may trace different parameters. The $J = 7_K \rightarrow 6_K$, $v_t = 0$, band is sensitive to both temperature and density (Leurini et al. 2004). However, infrared pumping can mimic the excitation effects of high density in the $v_t = 0$ state. Therefore, to distinguish between infrared pumping and density the torsionally excited $v_t = 1$ state should ideally be observed too (Leurini et al. 2007). Maser models show that maser emission can occur over a range of specific conditions (Sobolev & Deguchi 1994, Sobolev et al. 1997, Cragg et al. 2005). The 6.7 GHz maser is the most commonly occurring and generally brightest among a number of CH_3OH maser transitions. For the infrared pumping to be effective, dust temperatures exceeding 100 K are required, and for maser emission velocity specific column densities between a few times 10^{11} and 10^{14} cm^{-3}s are necessary. Furthermore, for densities $> 10^9$ cm^{-3} the maser is quenched by collisional de-excitation. To a lesser extent the gas temperature also influences the brightness temperature of the maser, with higher gas temperatures leading to a reduction of the brightness temperature.

Clearly for the maser emission to occur an enhanced (relative to pure gas-phase chemistry $\sim 10^{-11}$) CH_3OH abundance is required. The CH_3OH molecules form in the icy mantles of dust grains at low temperatures (∼10 K) by hydrogenation of CO (Watanabe et al. 2003, 2004, Fuchs et al. 2009) and evaporate off the dust grains as they warm up at ∼100 K (Collings et al. 2004). Alternatively, photo-desorption by UV photons may enhance the methanol abundance. As the protostar ignites and starts to ionise its environment the radiation will start to break down the methanol molecules. Therefore the methanol enhancement is thought to be very short (a few 10^4 years) and can serve as a chemical clock of the region (van der Tak et al. 2000a). The excitation of the 6.7 GHz methanol maser is through infra-red pumping and thus at least at the site of the methanol maser the radiation field cannot be neglected. To study the small scale distribution and excitation of the gas at the site of the methanol maser interferometric observations at mm and sub-mm wavelengths are required (e.g. Beuther et al. 2007b).

Ever since their discovery the 6.7 GHz methanol maser was found to be associated with high-mass star-formation because of its association with other maser species (OH

and H_2O) and ultra-compact H II (UCHII) regions (Menten 1991a). Initial surveys targeted IRAS sources and other maser sites, though the detection rate was not always particularly high (Schutte et al. 1993, Gaylard & MacLeod 1993, Caswell et al. 1995, van der Walt et al. 1995, Szymczak et al. 2000). The first blind survey by Ellingsen et al. (1996) showed that many methanol masers were not exclusively associated with IRAS sources and had colours different from typical UCHII regions. More recent studies have shown that the 6.7 GHz maser is generally associated with mm dust continuum ($> 95\%$) and much less frequently with cm emission ($\sim 25\%$) (Walsh et al. 1998, Beuther et al. 2002, Walsh et al. 2003, Hill et al. 2005). Breen et al. (2010) propose an evolutionary sequence in which, apart from the mm dust continuum, a weak 6.7 GHz CH_3OH maser is one of the first indicators of the high mass star-forming object. As the young star evolves and increases in luminosity, thus warming up its environment, the density decreases, and the brightness of the 6.7 GHz maser increases. After some 2×10^4 years a 12.2 GHz maser also forms and the source may be detectable in free-free emission at centimetre wavelengths. At this stage the OH maser turns on and after another 2×10^4 years the methanol masers disappear as the star continues to ionise its environment. Alongside the methanol masers water maser emission may be found in the outflow or shocked regions. Much effort is currently being spent on complete blind surveys of the 6.7 GHz methanol maser and follow-up programs (Green et al. 2010, Caswell et al. 2010, Pandian et al. 2011).

Our goal is to study the thermal methanol distribution and excitation in sources that exhibit 6.7 GHz methanol maser emission. We have started by studying the large scale characteristics of these regions. Consequently we have performed JCMT HARP-B observations of the $J = 7_K \rightarrow 6_K$, v_t=0, transition band of methanol at 338 GHz towards 13 sources with 6.7 GHz methanol masers, Table 4.1. The sources were initially selected from a sample of 12 relatively nearby, infrared bright 6.7 GHz sources studied at high resolution with the European VLBI Network (EVN). Due to scheduling constraints and to include a few more distant sources four other methanol maser sources mapped with the EVN were included from the sample of Bartkiewicz et al. (2009) even though their exact nature was uncertain at that point. The details of the observation procedure and data reduction are the same as for Cepheus A, described in Chapter 3. In this chapter we present the results of the remaining 13 sources and a statistical analysis of the complete sample.

4.2 Observations and data reduction

The JCMT[1] observations of the sources in this chapter were taken in 2007 and 2008 on the dates listed in Table 4.1 in the three observing programmes M07AN16, M07BN04, and M08AN10. We used the 16 element array receiver HARP and the observations were performed in a jiggle-chop mode (harp5) to create $2' \times 2'$maps with a pixel spacing of $6''$. This ensures proper Nyquist sampling of the $14''$ JCMT beam at 338 GHz. During the observations regular pointings were done on calibrators and we estimate an absolute

[1]The James Clerk Maxwell Telescope is operated by the Joint Astronomy Centre on behalf of the Science and Technology Facilities Council of the United Kingdom, the Netherlands Organisation for Scientific Research, and the National Research Council of Canada.

pointing accuracy of $\sim 1''$. In two cases, G23.657 and G24.541, the initial mapping scans showed the methanol emission to be constrained to a small area and very weak < 0.2 K, so for these two sources single pointing observations were done with the best receptor at the source.

The ACSIS correlator backend was set up with a bandwidth of 1 GHz (880 km s^{-1}) (at the time of the observations the 2 GHz bandwidth was not available) and 2048 channels centred on the CH_3OH $7_0 \rightarrow 6_0$ A^+ line at 338.41 GHz. The set-up covers 25 methanol lines in the $7_k \rightarrow 6_k$ band with a velocity resolution of 0.43 km s^{-1}, see Table 4.2 for details of the individual transitions. In our analysis we have adopted a main beam efficiency of 0.6 (Buckle et al. 2009) and estimate a calibration uncertainty of 20%.

The initial data inspection and re-gridding of the data was done with the Starlink package using Gaia/SPLAT after which the data were converted to GILDAS/CLASS format and the remaining data reduction and analysis was performed in CLASS. In order to increase the signal to noise of the spectra the data were smoothed to a velocity resolution of 0.87 km s^{-1} after which a linear baseline was fitted to the emission free regions of each spectra and subtracted. The analysis was then performed on a pixel by pixel basis in which the strongest unblended line in the spectra (-1E) was fitted with a Gaussian. The velocity of the -1E line was then used to calculate the velocities of the other 24 methanol lines. Around each calculated velocity the moments were calculated within a window size of two times the line width of the fitted -1E line.

The CH_3OH +1E line is potentially blended with the SO_2 $20_{4,19} \rightarrow 19_{2,18}$ at 338.61 GHz. However, the SO_2 $18_{4,14} \rightarrow 18_{3,15}$ at 338.31 GHz, which has a similar line strength and upper level energy, is not detected in most of our spectra. Therefore the contamination of the CH_3OH line by SO_2 is probably small in these sources.

The observations of DR21 were initially performed in alt-az beam-switching. In this region the emission extends in the North-South direction resulting in the off beam switching into an area with methanol emission at the same or similar velocity as in the region of interest. The observing program was modified to switch in East-West direction instead. The absorption features caused by the off beam switching into emission have been inspected and do in the end not influence the measurements.

Like in Chapter 3 we continue with a rotation diagram analysis for all pixels with at least three lines above our 6σ detection limit, and we have used the first and second moment of the lines to help determine whether the line is an actual detection. The velocity of the line is not allowed to deviate more than 1 km s^{-1} from the expected line velocity as determined by the fitting of the -1E line. Similarly the second moment may not deviate from the measured line width of the -1E line by more than 1 km s^{-1}. In the case of the complex emission of DR21, we have accepted the first and second moments to deviate up to 2 km s^{-1}.

Table 4.1: Sources and observing details. The observing dates are in yymmdd format.

Source	RA (J2000)	DEC (J2000)	d (kpc)	Luminosity ($L_\odot$)	Observing date
AFGL5142	+05:30:45.60	+33:47:52.0	1.8 [a]	4×10^3	070813
DR21(OH)	+20:39:00.40	+42:24:37.0	1.45 [b]	10^4	080730
G23.207−00.377	+18:34:55.20	-08:49:11.0	4.6 [c]	$< 10^4$	070617
G23.389+00.185	+18:33:14.33	-08:23:57.4	4.5 [c]	10^4	070617, 080731
G23.657−00.127	+18:34:51.56	-08:18:21.4	3.19 [d]	6×10^3	070617, 080801
G24.541+00.312	+18:34:55.72	-07:19:06.6	5.7 [c]	$< 10^4$	080729, 080730, 080802
G40.62−0.14	+19:06:01.609	+06:46:37.15	2.3 [e]	3×10^3	080622, 080729, 080731
G73.06+1.80	+20:08:10.10	+35:59:24.0	4.9 [f]	3×10^3	080729, 080730, 080731
G78.12+3.63	+20:14:26.1	+41:13:31	1.64 [g]	10^4	070708
L1206	+22:28:52.1	+64:13:43	0.776 [h]	900	070602, 070616, 070708, 080801
S255	+06:12:54.5	+17:59:20	1.59 [h]	2×10^4	080115
W3(OH)	+02:27:03.8	+61:52:25	1.95 [i]	8×10^4	070812

Notes: The coordinates are the actual observed coordinates and in the case of AFGL5142 the maser position is offset $\sim 30''$ to the East. [a]Snell et al. (1988), [b]Rygl et al. (2011), [c]Bartkiewicz et al. (2009), [d]Bartkiewicz et al. (2008), [e]This chapter, [f]Molinari et al. (2002), [g]Moscadelli et al. (2011), [h]Rygl et al. (2010), [i]Xu et al. (2006).

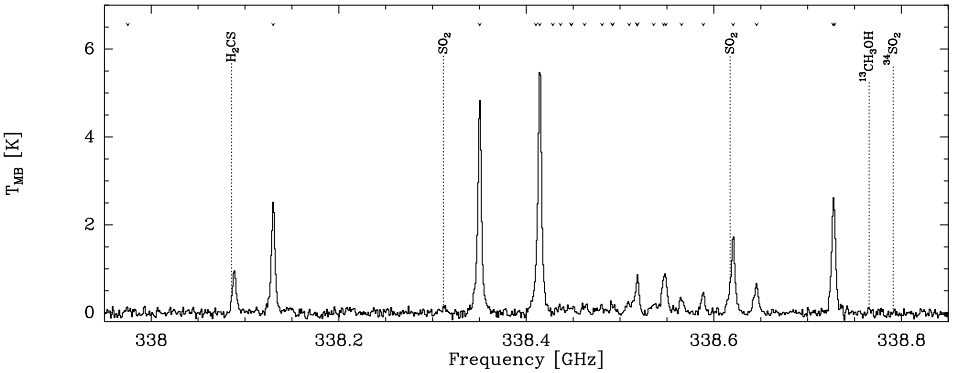

Figure 4.1: *AFGL 5142:* Spectrum of the maser position indicated in Fig. 4.2. The tick marks at the top indicate the frequencies of the methanol lines.

4.3 Results

In this section we discuss the results on the individual sources, starting with a brief background on the sources with emphasis on the aspects relevant for this chapter, like information on distance to the source, orientation, and occurrence of outflows etc. For each source the morphology of the CH_3OH $-1E$ line emission is described and the results of the rotation diagram analysis are summarised in Table 4.3.

4.3.1 AFGL 5142

Observations of cm and mm continuum indicate that AFGL 5142 is a zero-age main sequence (ZAMS) B2 star with a luminosity of 4×10^3 $L_\odot$ (Zhang et al. 2002) at a distance of 1.8 kpc (Snell et al. 1988). Zhang et al. (2007) identify five mm continuum peaks (MM-1 − MM-5) and three cm continuum peaks (CM-1A, CM-1B, and CM-2) within 4″. MM-1 and MM-2 appear to be more massive (both 4×10^3 to 7×10^4 $L_\odot$) and/or evolved than MM-3 − MM-5 although only MM-1 and MM-3 are associated with cm continuum emission. Molecular line observations of CH_3CN show that MM-2 ($v_{LSR} = -3.4\,km\,s^{-1}$) has a much higher temperature and column density than MM-1 ($v_{LSR} = -1.0\,km\,s^{-1}$) suggesting that MM-2 is in a more evolved state even though it is not associated with cm continuum emission (Zhang et al. 2007). The 6.7 GHz CH_3OH maser position is located between the two cm continuum peaks 1A and 1B associated with MM-1 (Goddi et al. 2007). Early CO(2-1) and CO(3-2) studies reveal an outflow in the North-South direction associated with the mm continuum emission, unresolved in single-dish data (Hunter et al. 1995). Interferometric imaging shows at least three different outflows associated with the mm continuum peaks. Zhang et al. (2007) identify the North-South outflow (A, PA=5°) with MM-2, a second outflow (B, PA=35°) with MM-3, and the third (C, PA=-60°) with MM-1.

Table 4.2: CH_3OH ($7_K \rightarrow 6_K$) line data for the observed transitions.

Frequency (MHz)	$\mu_g^2 S_g$ (D^2)	E_u (K)	Transition K type	
337969.414	5.55	390.1	−1 A	ν_t=1
338124.502	5.65	78.1	0 E	
338344.628	5.55	70.6	−1 E	
338404.580	1.49	243.8	+6 E	
338408.681	5.66	65.0	0 A	
338430.933	1.50	253.9	−6 E	
338442.344*	1.49	258.7	+6 A	
338442.344*	1.49	258.7	−6 A	
338456.499	2.76	189.0	−5 E	
338475.290	2.76	201.1	+5 E	
338486.337*	2.77	202.9	+5 A	
338486.337*	2.77	202.9	−5 A	
338504.099	3.80	152.9	−4 E	
338512.627*	3.81	145.3	−4 A	
338512.639*	3.81	145.3	+4 A	
338512.856*	5.23	102.7	−2 A	
338530.249	3.82	161.0	+4 E	
338540.795*	4.60	114.8	+3 A	
338543.204*	4.60	114.8	−3 A	
338559.928	4.64	127.7	−3 E	
338583.195	4.62	112.7	+3 E	
338614.999	5.68	86.1	+1 E	
338639.939	5.23	102.7	+2 A	
338721.630	5.14	87.3	+2 E	
338722.940	5.20	90.9	−2 E	

Notes: All lines are from the $J = 7 \rightarrow 6$ band, and throughout the chapter a notation like "−6 E" refers to the $J = 7_{-6} \rightarrow 6_{-6}$ E transition. Blended lines are indicated by a *. Adopted from the CDMS (Cologne Database of Molecular Spectroscopy, Müller et al. (2005)).

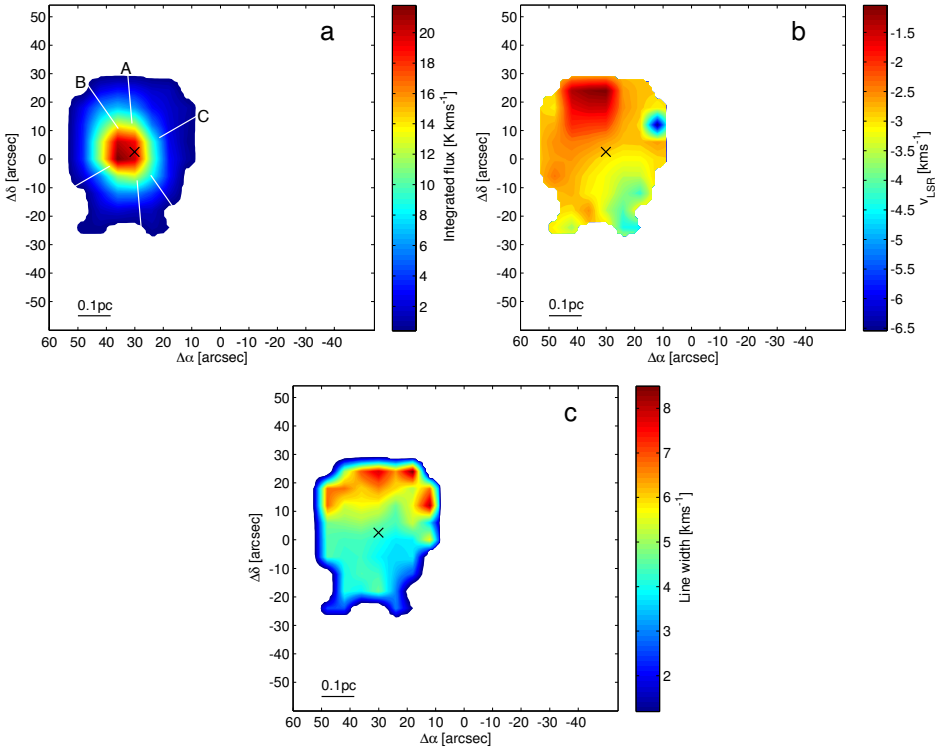

Figure 4.2: Integrated intensity (a), central velocity (b) and FWHM width (c) of the CH_3OH $7(-1) \rightarrow 6(-1)$ E line observed toward AFGL 5142. The black cross marks the position of the 6.7 GHz maser and the outflow directions A, B, and C (Zhang et al. 2007) are indicated by the white lines.

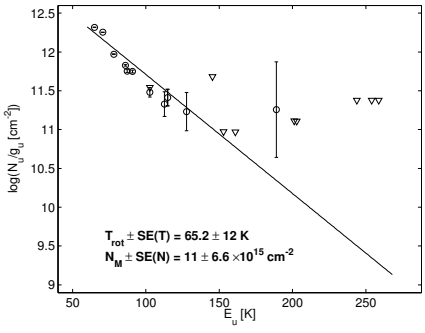

Figure 4.3: *AFGL 5142:* Rotation diagram of CH_3OH for the position of the maser.

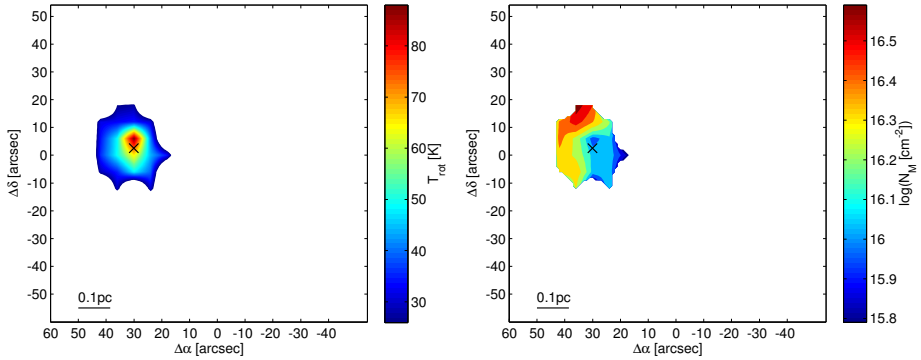

Figure 4.4: *AFGL 5142:* Maps of CH_3OH rotation temperature and column density.

The observations of AFGL5142 were performed at the wrong coordinates (offset by ∼30″) and therefore the maser (indicated by the black cross) and CH_3OH emission do not appear in the centre of the map. The CH_3OH emission (Figs. 4.2 a-c) is constrained to a roughly circular area with a clear peak intensity of the −1E line in the centre, close to the position of the methanol maser ($\Delta\alpha$=+30.1″, $\Delta\delta$=+2.6″). The velocity map shows a bipolar velocity field with redshifted velocities to the NE and blueshifted velocities to the SW. The blueshifted spot to the NW of the maser position is probably not significant. The line width map indicates that the line widths are larger to the North than to the South, however this may be due to lower signal-to-noise to the North.

The spectrum from the maser position in AFGL5142 (Fig. 4.1) shows that lines up to K=3 are detected. There is no detection of the vibrationally excited line (v_t = 1). There is some SO_2 emission, but it is at most 10% of the K=+1E flux and it is offset in velocity. Since we only integrate an area two times the line width the contribution of SO_2 to the K=+1E flux is negligible. Therefore we include the K=+1E line in the analysis. We find rotation temperatures between 26.0 and 88.5 K, and column densities between 6.3×10^{15} and 4.0×10^{16} cm^{-2} across the map. The highest rotation temperatures are associated with the position of the methanol maser, Fig. 4.4a. There seems to be a column density gradient across the source with higher column densities associated with the redshifted emission to the NE and lower column densities associated with the blueshifted emission to the SW, Fig. 4.4 b.

4.3.2 DR21 (FIR1 & FIR2)

DR21(OH)N is part of the DR21-W75 filament in the Cygnus X region. The complex has a parallax distance of 1.45 kpc (Rygl et al. 2011) and the dense massive core (C160) that both FIR1 and FIR2 are associated with has a total luminosity of 1.1×10^4 $L_\odot$ (Roy et al. 2011). The massive core consists of five mm clumps and the 6.7 GHz CH_3OH masers FIR1 and FIR2 are associated with the clumps N43 and N51 respectively (Motte et al.

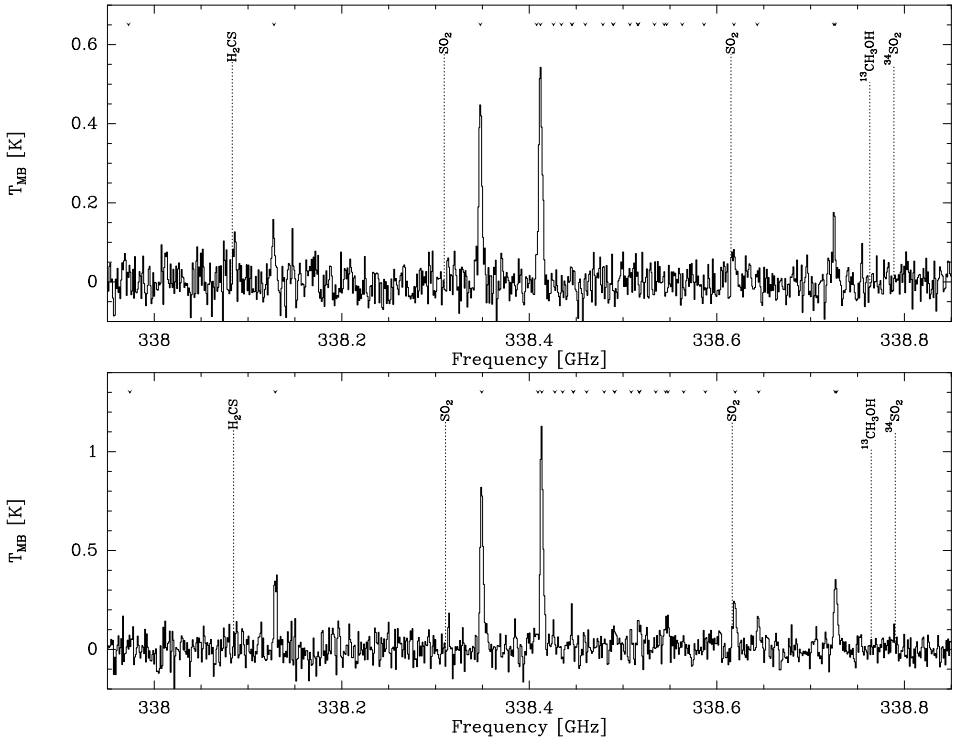

Figure 4.5: *DR21: Top:* Spectrum of the FIR1 maser position.*Bottom:* Spectrum of the FIR2 maser position. The tick marks at the top indicate the frequencies of the methanol lines.

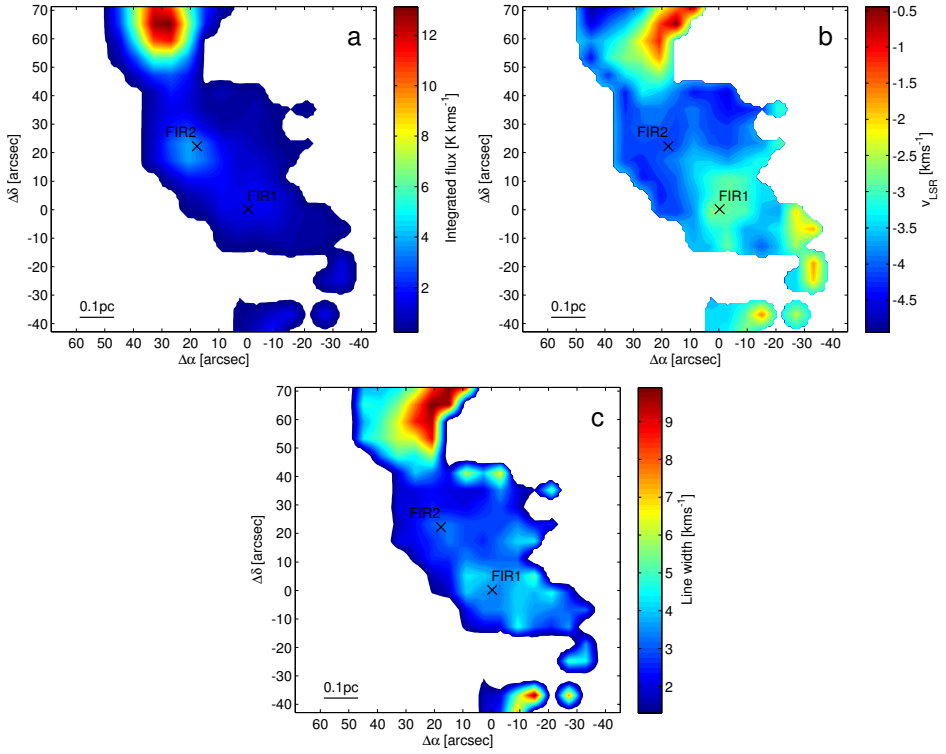

Figure 4.6: As Fig. 4.2 for the source DR21.

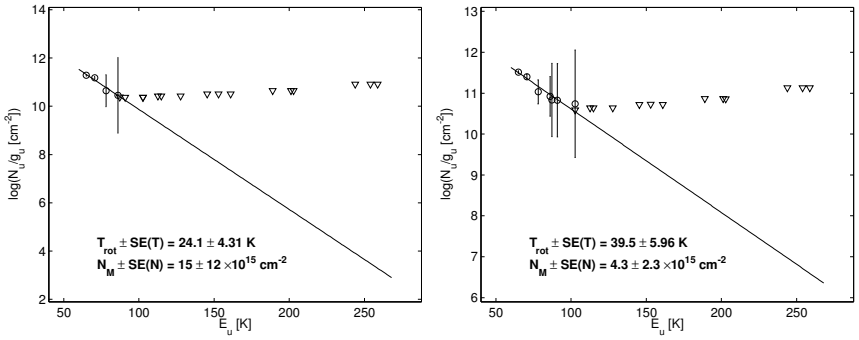

Figure 4.7: *DR21:* Rotation diagrams of CH_3OH for the positions of the masers. *Left:* FIR1. *Right:* FIR2.

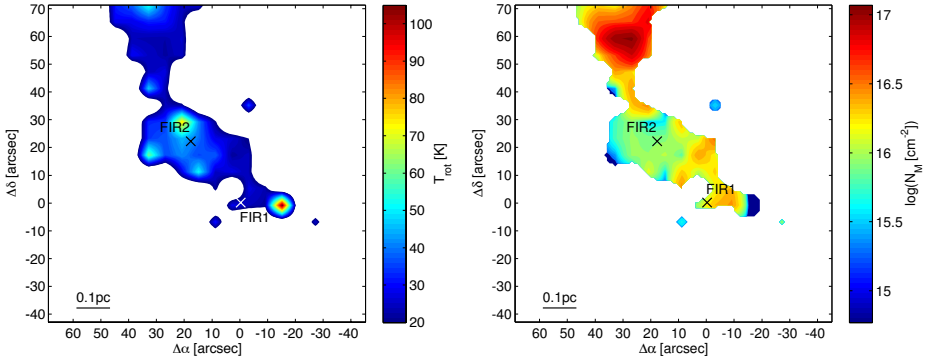

Figure 4.8: *DR21:* Maps of CH_3OH rotation temperature and column density.

2007). The source FIR1 has a luminosity of ∼1400 $L_\odot$ (Chandler et al. 1993). Several molecular outflows have been observed as well as multiple H_2 knots (Davis et al. 2007, Schneider et al. 2010, 2006).

In DR21, the CH_3OH −1E line emission shows that the emission extends in a large structure from South to North with the brightest emission to the North, Figs. 4.6 a-c. The two maser positions FIR1 ($\Delta\alpha$=-0.3″, $\Delta\delta$=+0.1″) and FIR2 ($\Delta\alpha$=+17.6″, $\Delta\delta$=+22.3″) are located in the central region of the map. The velocity field map is complex and does not show any clear indication of a simple velocity gradient in the area of the maser emission. The line width map shows a maximum in the North in the region of the source FIR3 (Motte et al. 2007), the lines in this area of the map are asymmetric.

The spectra of the two maser regions FIR1 and FIR2 (Fig. 4.5) show that lines up to K=1 and K=2 are detected. The v_t = 1 line is not detected. We do not observe any SO_2 emission at either position and therefore include the +1E line in the rotation diagram analysis. In the rotation diagram analysis we use a SNR cut-off of 4 and a maximum velocity and width difference of 2 km s^{-1} between the expected velocity/width and the calculated moments. However, because we focused on the maser positions during the observations, the emission to the North, where the lines are not Gaussian cannot be analysed properly.

The results of the rotation diagram analysis are illustrated by the the rotation temperature and column density maps (Figs. 4.8 a-b). There is a rotation temperature maximum close to the source DR21 FIR2. In contrast, no enhanced rotation temperature is seen at the position of FIR1. The column density map shows an enhanced column density to the North of both maser sources but does not show any enhancement at either of the positions of the two masers.

4.3.3 G23.207−00.377

The source G23.207−00.377 has a MIR counterpart, and is associated with water masers, although no radio continuum has been detected (Bartkiewicz et al. 2011). Its distance is

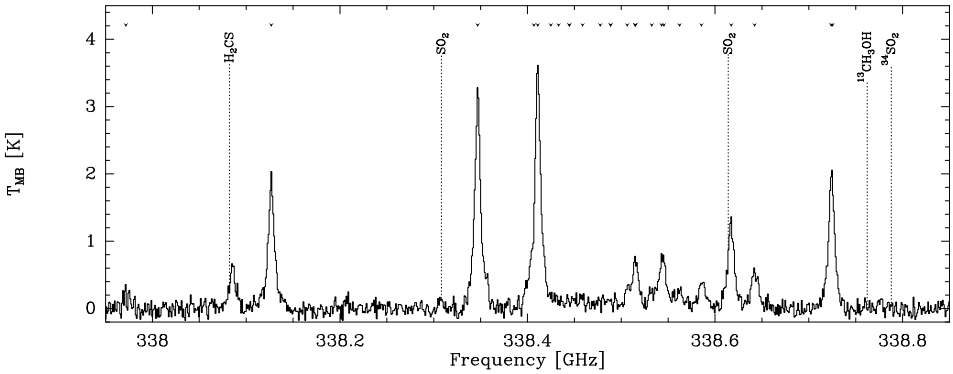

Figure 4.9: *G23.207−00.377:* Spectrum of the maser position.

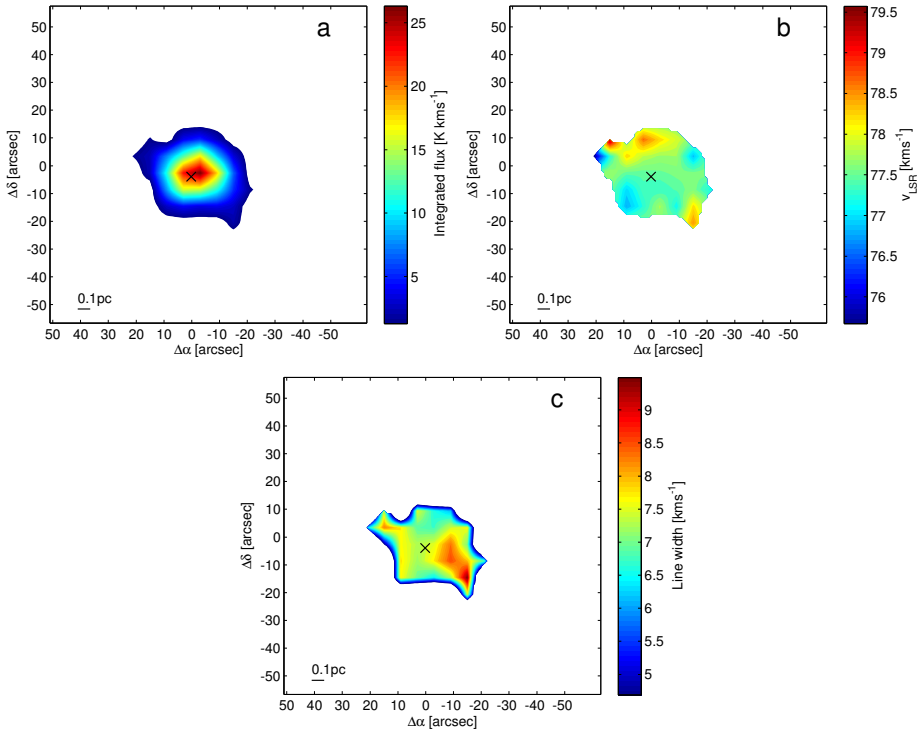

Figure 4.10: As Fig. 4.2 for the source G23.207−00.377.

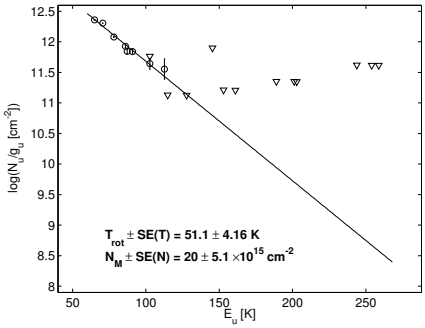

Figure 4.11: *G23.207−00.377:* Rotation diagram of CH_3OH for the maser position.

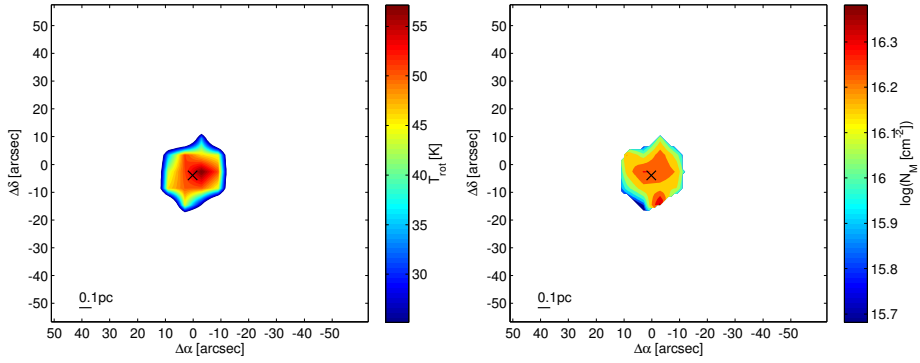

Figure 4.12: *G23.207−00.377:* Maps of CH_3OH rotation temperature and column density.

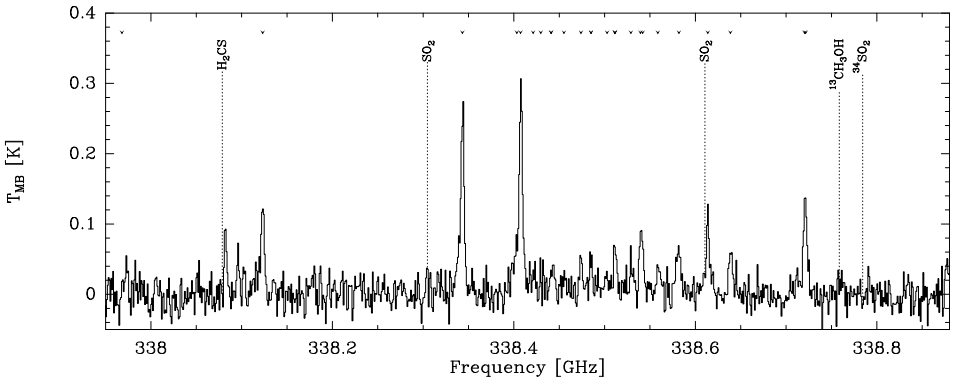

Figure 4.13: *G23.389+00.185:* Average spectrum of the four centre pixels of the maser position. The tick marks at the top indicate the frequencies of the methanol lines.

estimated to 4.6 kpc by Bartkiewicz et al. (2009) based on the kinematic distance model of Reid et al. (2009b). Using the IRAS fluxes we have estimated the luminosity of the source to $< 10^4$ $L_\odot$ using eq. 3 in Walsh et al. (1997), though the non-detections at 60 and 100 μm make not only the luminosity uncertain, but also its identification as a high-mass star-forming region.

The CH_3OH −1E line emission in G23.207−00.377 (Figs. 4.10) is confined to within 20″ radius from the source with a clear maximum in the centre of the map close to the position of the maser ($\Delta\alpha$=+0.2″, $\Delta\delta$=-3.9″). The maps of the velocity field and the line width do not show a clear structure, probably as a result of a low signal-to-noise ratio.

The spectra of the maser position (Fig. 4.9) show that lines up to K=2 are detected. There is also an emission feature tentatively identified with the v_t = 1 line. The SO_2 emission is weak and we have therefore included the k=+1E line in the analysis. The rotation temperature and column density of the maser position are reported in Table 4.3. Similar to the CH_3OH −1E line flux, both the rotation temperature and column density in G23.207−00.377 (Figs. 4.12 a-b) show a maximum close to the position of the maser.

4.3.4 G23.389+00.185

G23.389+00.185 has a near kinematic distance of 4.5 kpc, it has a MIR counterpart and a luminosity if 10^4 $L_\odot$ (Bartkiewicz private communication). It is associated with water maser emission though no radio continuum emission has been detected (Bartkiewicz et al. 2011, 2009).

In G23.389+00.185 the CH_3OH emission is compact and confined to the central area with a clear maximum at the position of the maser ($\Delta\alpha$=+0.0″, $\Delta\delta$=0.0″), Figs 4.14 a-c. The velocity field map shows sign of a velocity gradient of 1.4 km s^{-1} pc^{-1} across the source with redshifted emission to the SE and blueshifted emission to the NW. The line width map does not show any features of particular interest.

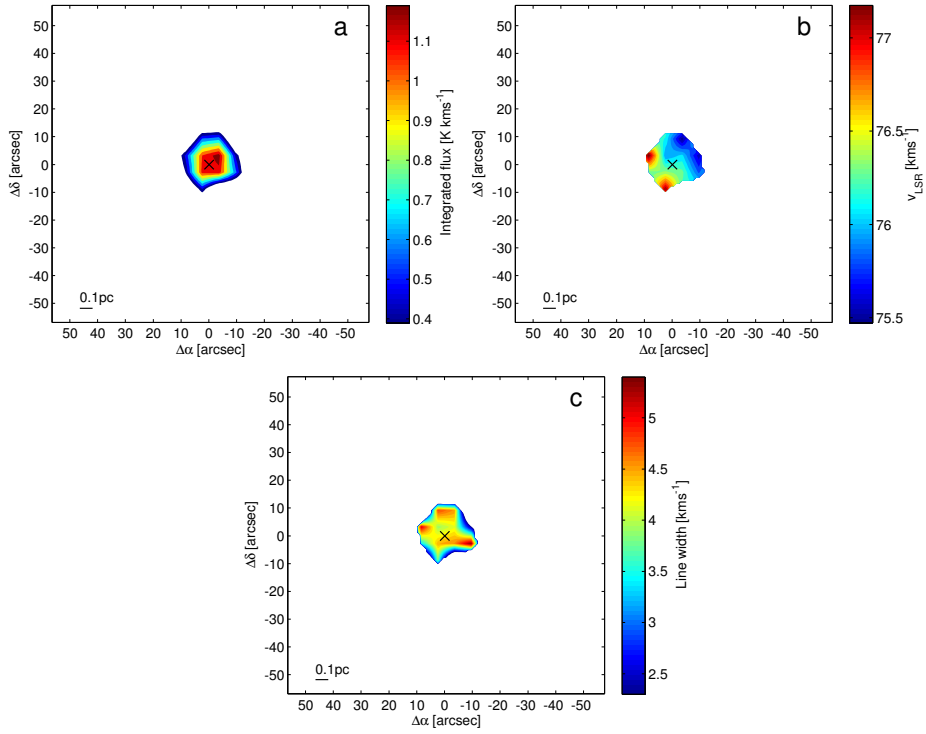

Figure 4.14: As Fig. 4.2 for the source G23.389+00.185.

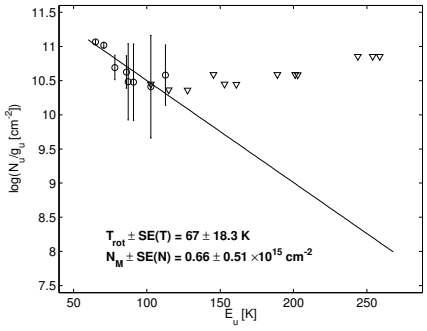

Figure 4.15: *G23.389+00.185:* Rotation diagram of the four averaged pixels at the position of the maser.

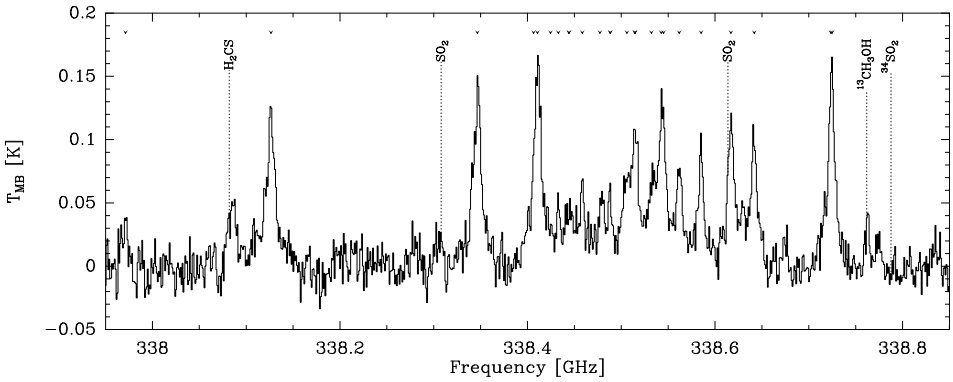

Figure 4.16: *G23.657−00.127:* Spectrum at the maser position. The tick marks at the top indicate the frequencies of the methanol lines.

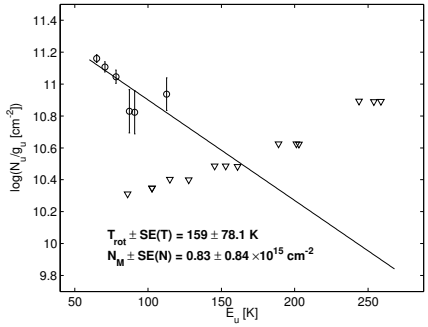

Figure 4.17: *G23.657−00.127:* Rotation diagram of CH_3OH for the position of the maser.

The extent of the CH_3OH emission is small and to improve the signal to noise the four centre pixels are averaged. The averaged spectrum (Fig. 4.13) shows the detection of lines up to K=2. There is a weak emission feature in the spectrum close to the frequency of the $v_t = 1$ line. The SO_2 line is not detected and consequently the +1E line is included in the analysis. We find a rotation temperature of 67 K and a methanol column density of $6.6 \times 10^{14}\,\mathrm{cm}^{-2}$.

4.3.5 G23.657−00.127

The conspicuous ring source G23.657−00.127, characterised by its ring-distribution of 6.7 and 12.2 GHz CH_3OH maser emission, has a parallax based distance estimate of 3.19 kpc (Bartkiewicz et al. 2008, 2005b), considerably closer than its (near) kinematic distance of ∼5 kpc. It has an infrared counterpart and its SED suggests a luminosity of

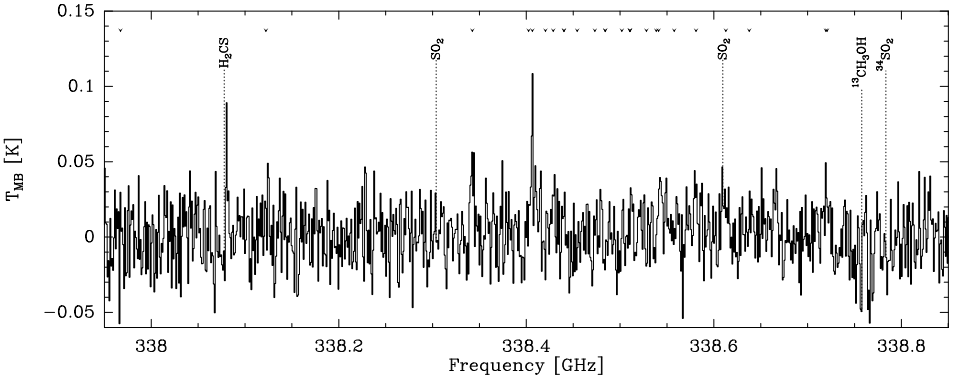

Figure 4.18: *G24.541+00.312:* Spectrum of the maser position. The tick marks at the top indicate the frequencies of the methanol lines.

6×10^3 $L_\odot$ (Bartkiewicz, priv. communication), equivalent to a single B1 ZAMS star (Panagia 1973). The source does not have water maser or radio continuum emission association (Bartkiewicz et al. 2009, 2011).

The CH_3OH emission in G23.657−00.127 is weak and compact and we are therefore unable to map the distribution as we have done for the other sources. Instead the source was observed in a single pointing mode in which the receptor was centred on the position of the maser emission for a deep integration. The resulting spectrum (Fig. 4.16) is complex and suffers from line blending. Because of the line blending only lines up to K=2 are included in the analysis, though higher K lines contribute to the spectrum. Also the $v_t = 1$ line is detected. There may be some SO_2 emission but it does not seem to contribute significantly to the measured CH_3OH flux and the +1E line is therefore included in the analysis. We find a rotation temperature of ∼160 K and a column density of $\sim 10^{15}$ cm^{-2}, however, there appears to be multiple velocity components that we are unable to separate and therefore the complexity of the spectrum violates the assumptions we use for the statistical approach in this chapter. In the rotation diagram (Fig. 4.17) several of the lines have upper limits below the fitted line, but we have chosen to disregard these because of the line blending.

4.3.6 G24.541+00.312

G24.541+00.312 has a near kinematic distance of 5.70 kpc. It has a MIR counterpart but no close association with water masers or detected radio continuum (Bartkiewicz et al. 2009, 2011). The source luminosity is estimated in the same manner as for G23.207−00.377, Sec. 4.3.3. We find a luminosity of $< 10^4$ $L_\odot$ though the non-detections at 60 and 100 μm make not only the luminosity uncertain, but also its identification as a high-mass star-forming region.

Also in G24.541+00.312 the CH_3OH emission is weak < 0.1 K and unresolved, and

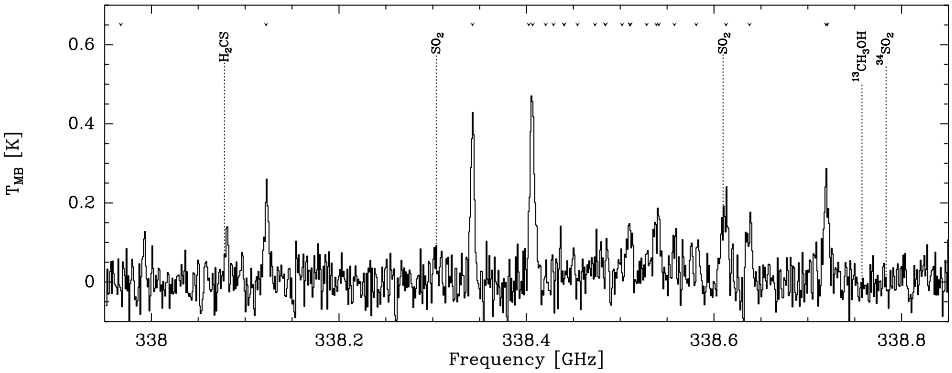

Figure 4.19: *G40.62−0.14:* Spectrum of the maser position.

after the initial mapping attempts the single pointing mode was used to acquire the data. Due to the poor signal to noise we have excluded this source from the analysis and only show the spectrum here for completeness, Fig. 4.18.

4.3.7 G40.62−0.14

In recent literature two different distances for G40.62−0.14 are used: 2.2 kpc (López-Sepulcre et al. 2010) and 10.5 kpc (Pandian et al. 2009). To be consistent we have calculated the kinematic distance using the model of Reid et al. (2009b). We find a kinematic distance of 2.3 kpc, similar to the distance adopted by López-Sepulcre et al. (2010) and the source has a luminosity of 2.5×10^3 $L_\odot$ scaled from the kinematic far distance (Pandian et al. 2009, 2010). The source has a $\sim 30''$ bipolar molecular outflow oriented SE (blue) - NW (red) (López-Sepulcre et al. 2010). The radio continuum source is detected at 1.3 cm and 6.9 mm, but not at 3.6 cm, which indicates that it may be a hyper-compact (HC) HII region. There is a second cm/mm source nearby (~2") consistent with an UCHII region (Pandian et al. 2010).

The CH_3OH −1E line emission in G40.62−0.14 (Figs. 4.20 a-c) is compact, and constrained to the centre of the map with a maximum near the position of the methanol maser ($\Delta\alpha$=+0.1″, $\Delta\delta$=+0.1″). The velocity map shows a velocity gradient with blueshifted emission to the SE and redshifted emission to the NW, consistent with previous observations (López-Sepulcre et al. 2010). To the SE of the maser position, in the blueshifted area, there is a maximum in the line width map, though it may be due to poor signal to noise.

The spectrum of the maser position (Fig. 4.19) shows that lines up to K=2 are detected. Higher-K lines and the v_t = 1 line are not detected. SO_2 is detected and seems to contribute a significant amount of flux to the +1E line and we have therefore excluded this line from the analysis. The results of the rotation diagram analysis at the maser position are listed in Table 4.3.

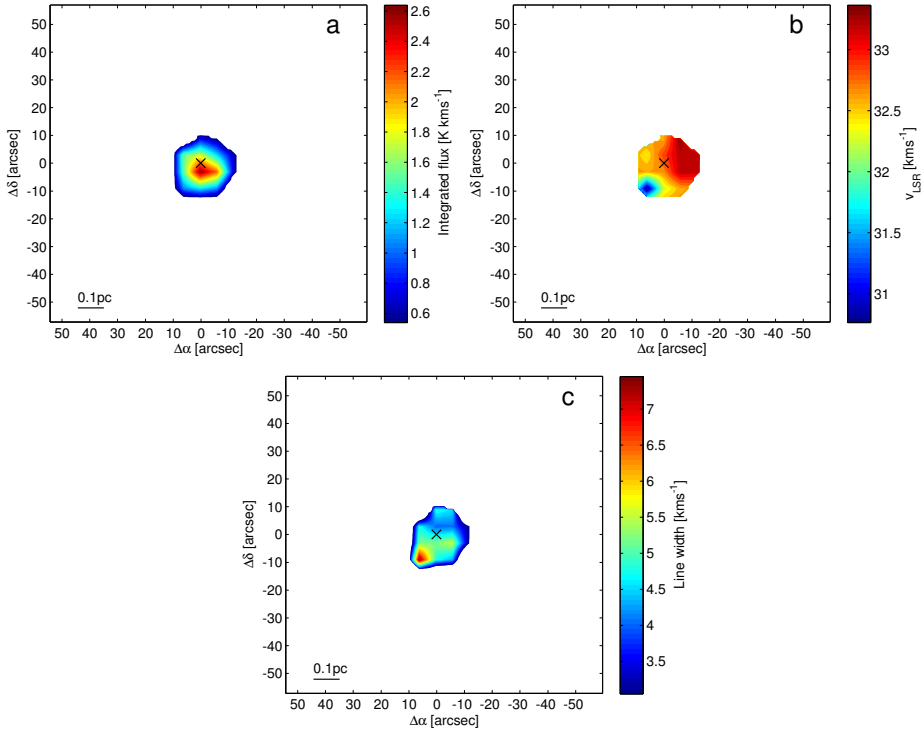

Figure 4.20: As Fig. 4.2 for the source G40.62−0.14.

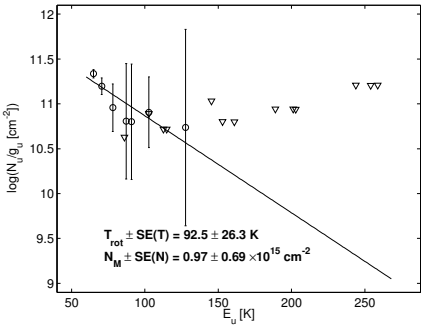

Figure 4.21: *G40.62−0.14:* Rotation diagram of CH_3OH at the position of the maser.

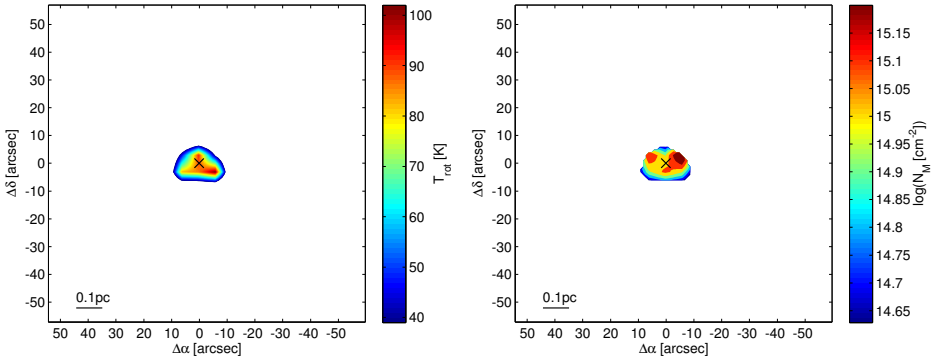

Figure 4.22: *G40.62−0.14:* Maps of CH_3OH rotation temperature and column density.

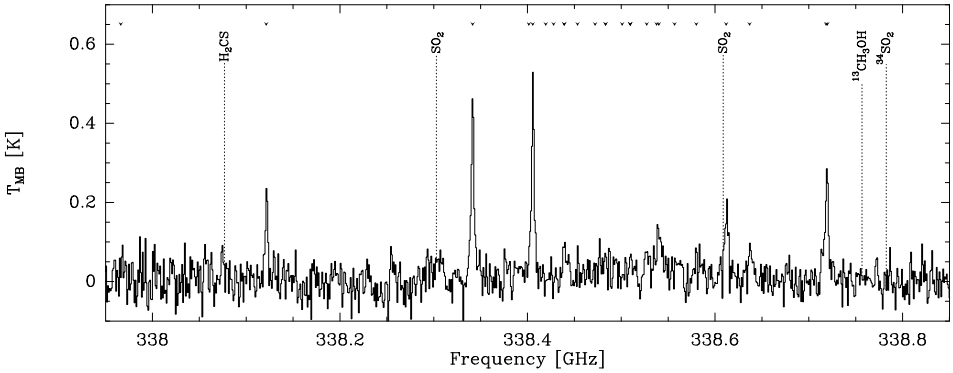

Figure 4.23: *G73.06+1.80:* Spectrum of the maser position. The tick marks at the top indicate the frequencies of the methanol lines.

4.3.8 G73.06+1.80

G73.06+1.80 has a luminosity of 3.2×10^3 $L_\odot$ at a kinematic distance of 4.9 kpc (Molinari et al. 2002), and is associated with both methanol and water masers. Although it shows a complex velocity field in HCO^+ it also has a bipolar outflow seen in CO, infrared, and H_2 (Zhang et al. 2005, Varricatt et al. 2010). The outflow is oriented NE (blue) - SW (red) and seems to originate from a faint infrared source < 0.5″ from the methanol maser position (Chapter 5).

In G73.06+1.80 the CH_3OH −1E line maps (Figs. 4.24 a-c) show that the emission is compact and constrained to the centre of our map with a maximum close to the maser position ($\Delta\alpha$=+0.1″, $\Delta\delta$=+0.1″). The velocity map shows a gradient with blueshifted emission to the E and redshifted emission to the W. The redshifted emission to the W is however associated with a maximum in the line width map and the single data point

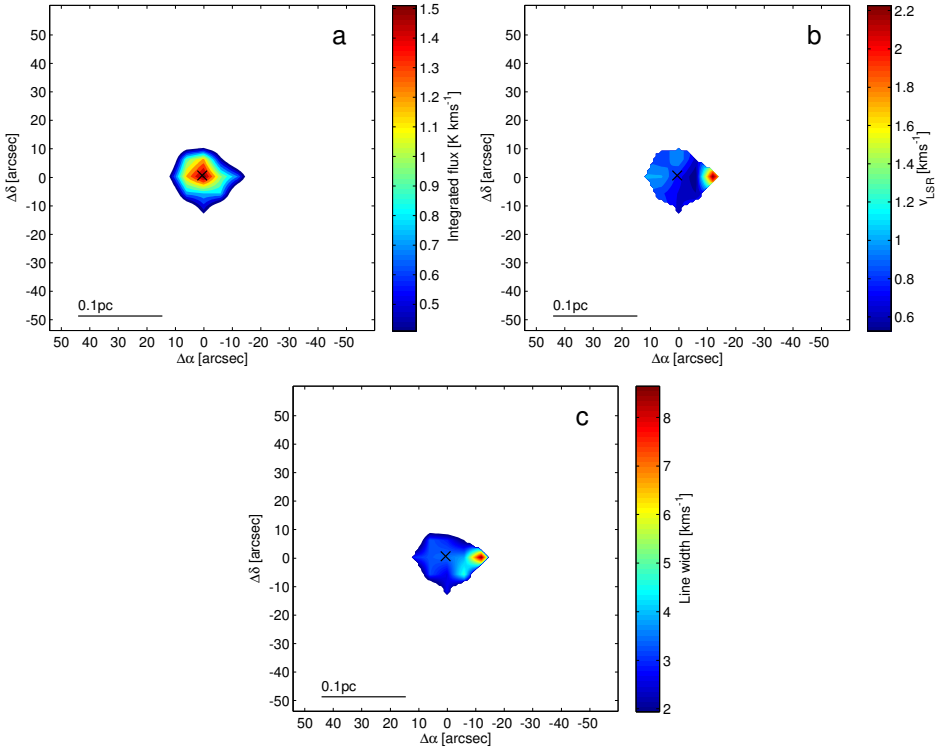

Figure 4.24: As Fig. 4.2 for the source G73.06+1.80.

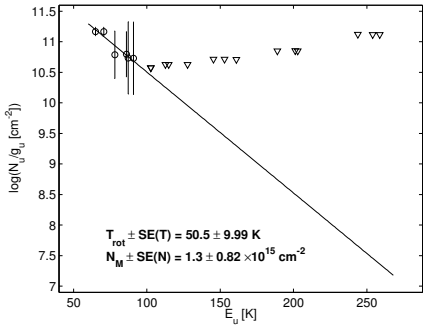

Figure 4.25: *G73.06+1.80:* Rotation diagram of CH_3OH for the position of the maser.

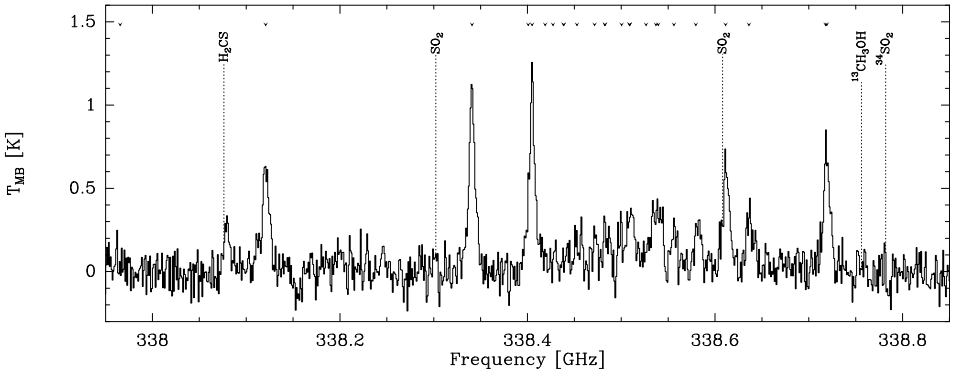

Figure 4.26: *G78.12+3.63:* Spectrum of the maser position. The tick marks at the top indicate the frequencies of the methanol lines.

responsible for it seems to be due to poor signal to noise.

The spectrum of the maser position (Fig. 4.23) shows that lines up to K=2 are detected. The contribution of SO_2 to the +1E line flux does not seem to be significant and we have included the line in the analysis. The signal to noise of our data does not allow us to map the excitation and only for the centre pixel can we perform a rotation diagram analysis, Fig. 4.25.

4.3.9 G78.12+3.63

G78.12+3.63 (IRAS 20126+4104) has been studied extensively at many different wavelengths, see Varricatt et al. (2010) for a recent comprehensive review. The object has a luminosity of 10^4 $L_\odot$ at a parallax distance of 1.64 kpc (Moscadelli et al. 2011). It has a molecular outflow that extends ~0.4 pc oriented to the NW (red) - SE (blue). At the origin of the outflow mm continuum emission is associated with a Keplerian disk seen in several molecular species, the disk is oriented roughly perpendicular to the outflow (Cesaroni et al. 1999, 2005).

The CH_3OH −1E line emission in G78.12+3.63 is constrained to the centre of the map and elongated in the SE/NW direction (Figs. 4.27a-c), consistent with the thermal CH_3OH being part of the molecular outflow. The integrated flux map shows a maximum close to the position of the methanol maser ($\Delta\alpha$=-0.6″, $\Delta\delta$=+1.7″). There is a clear velocity gradient of 13.1 km s^{-1} pc^{-1} in the direction of the outflow with blueshifted emission to the SE and redshifted emission to the NW. The line width map shows a maximum to the SE, associated with the blueshifted emission.

The spectra from the centre region (Fig. 4.26) are complex and suffer from line blending. The v_t = 1 is not detected but the flux from the SO_2 line in the centre region has led us to exclude the +1E line from the analysis. Lines up to K=2 are detected, though from the rotation diagram (Fig. 4.28) it is clear that the high-K line strengths are over estimated

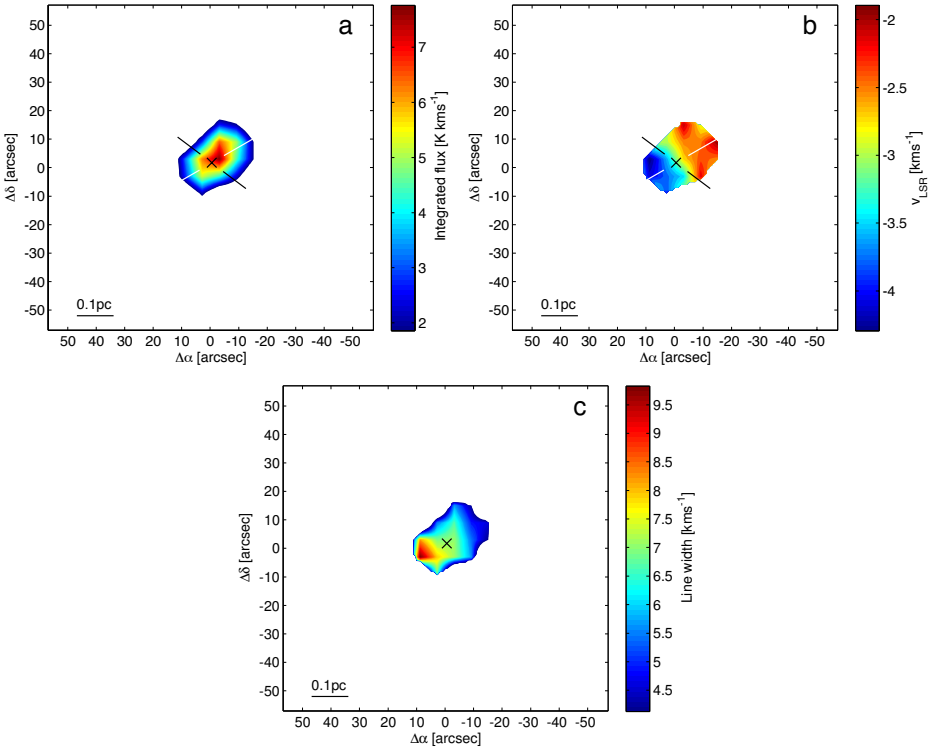

Figure 4.27: As Fig. 4.2 for the source G78.12+3.63. The white line indicates the direction of the outflow and the black line that of the disk (Cesaroni et al. 2005).

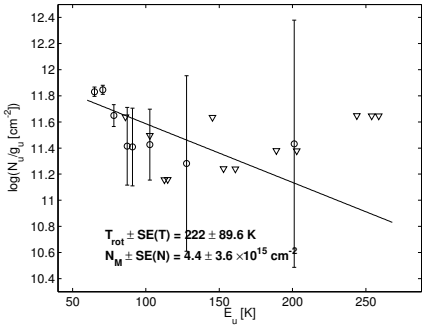

Figure 4.28: *G78.12+3.63:* Rotation diagram of CH_3OH for the position of the maser.

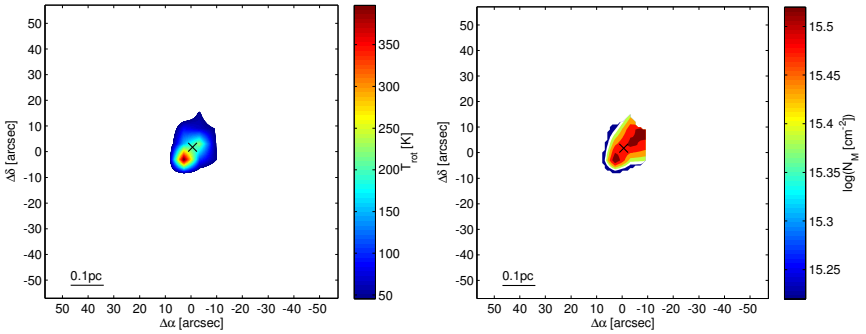

Figure 4.29: *G78.12+3.63:* Maps of rotation temperature and column density.

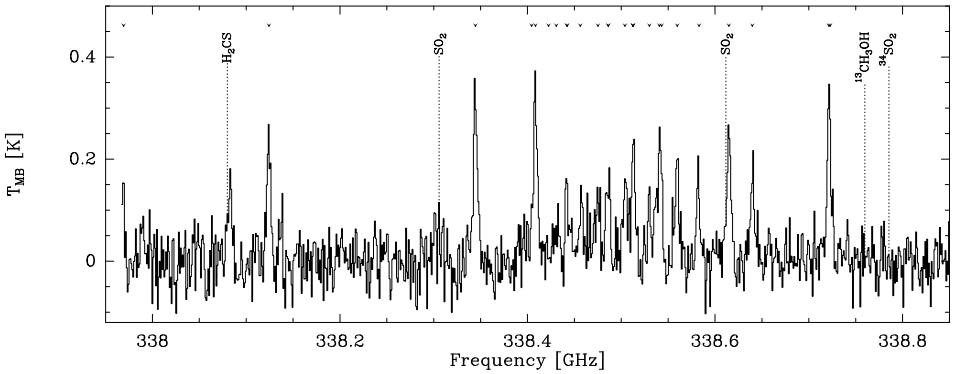

Figure 4.30: *L1206:* Spectrum of the maser position. The tick marks at the top indicate the frequencies of the methanol lines.

and we consider the rotation temperature as an upper limit. The rotation temperature shows a maximum associated with the blueshifted emission to the SE of the maser position (Fig. 4.29a). The column density map shows an enhancement both to the SE and to the NW of the maser position (Fig. 4.29b).

4.3.10 L1206

L1206 has a luminosity of 900 $L_\odot$ scaled to the parallax distance of 776 pc (Rygl et al. 2010). It has a systemic velocity of $v_{LSR} = 11\,km\,s^{-1}$ measured in $C^{18}O$ ($J = 1 \rightarrow 0$) and HC_3N ($J = 12 \rightarrow 11$) and a CO outflow (PA=140°) with blueshifted emission to the NW and redshifted emission to the SE (Beltrán et al. 2006). This is opposite to what we see in our velocity cut along the major axis. It could be consistent with our measurement of the

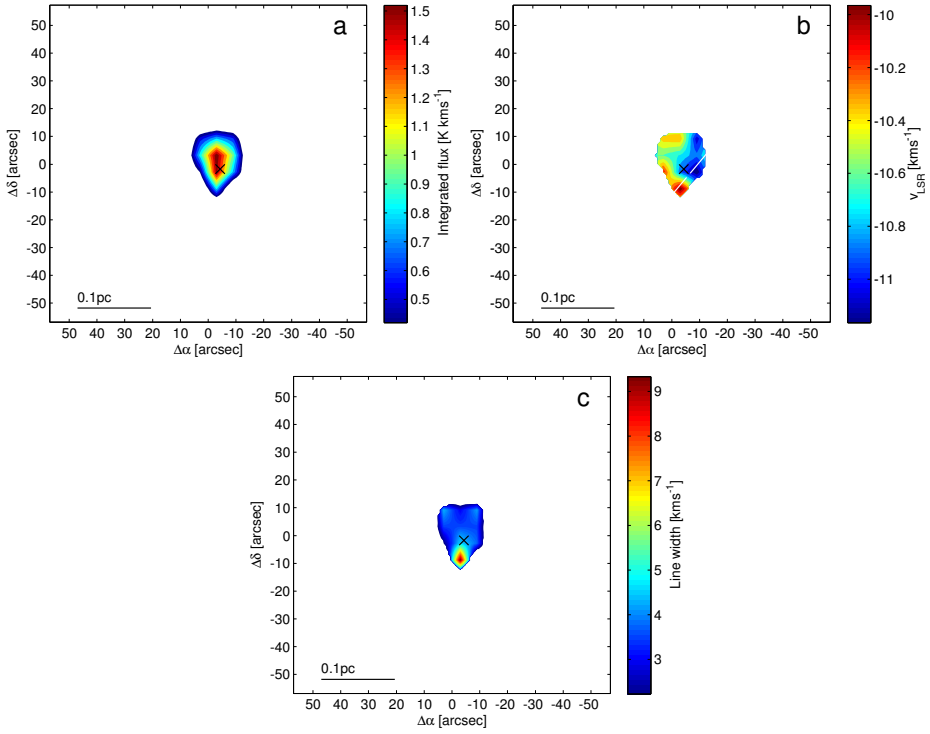

Figure 4.31: As Fig. 4.2 for the source L1206. The white line indicated the PA of the CO outflow.

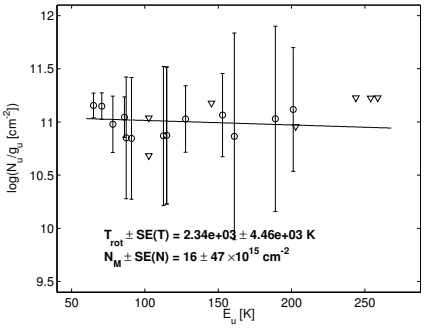

Figure 4.32: *L1206:* Rotation diagrams for the position of the maser.

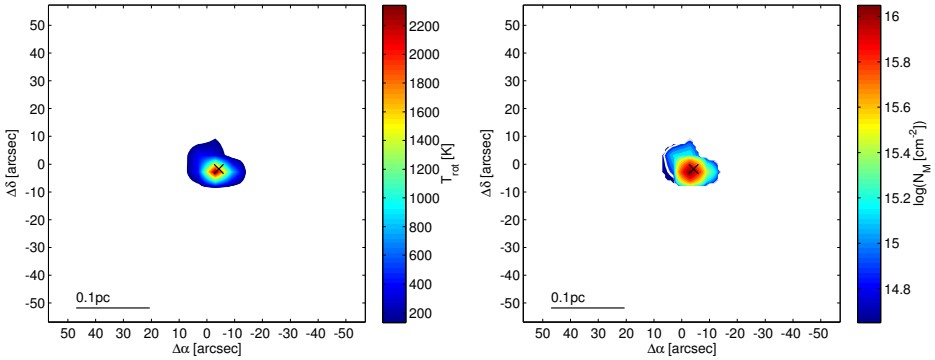

Figure 4.33: *L1206:* Maps of rotation temperature and column density.

velocity if the cut was made just to the South of the maser position at the same PA as the CO outflow (indicated in Fig. 4.31b).

During the data reduction process we discovered two issues with the data for L1206. First, the data acquired on the date 20070602 show large ripples in baselines of receptor R06. Second, the data taken on 20070616 show a pronounced broad "absorption" feature in some areas sampled by receptor R06. Consequently the data from receptor R06 in all twelve scans from these dates were flagged.

The CH_3OH −1E line emission (Figs. 4.31) is compact and constrained to the centre of the map with a maximum close to the position of the methanol maser ($\Delta\alpha$=-4.3″, $\Delta\delta$=-1.7″). The line velocity map shows the blueshifted emission to the W and the more redshifted emission to the S and SE. There is a maximum in the line width map to the S associated with the redshifted emission.

The spectrum from the centre region (Fig. 4.30) is noisy and suffers from line blending. The v_t = 1 line is detected but right at the band edge. We exclude high optical depth effects as being important because of the lack of $^{13}CH_3OH$ emission. The contribution of SO_2 looks to be small and we have therefore included the +1E line in the rotation diagram analysis. The data do not allow us to map the excitation and the rotation diagram analysis is restricted to the centre pixel (Fig. 4.32). Lines up to K=4 are detected with our detection criteria. However, as can be seen in the rotation diagram the low signal to noise and line blending leads to an unrealistically high (2300 K) rotation temperature, also the population diagram analysis (Sec. 4.4.3) is affected by this. Nevertheless, the conclusion that the rotation temperature is high (> 100 K) is secure.

4.3.11 S255

With a parallax distance estimate of 1.59 kpc (Rygl et al. 2010), S255IR is a high mass star forming complex situated between the HII regions S255 to the East and S257 to the West. S255IR consists of three UCHII regions, S255N, S255S, and S255IR. The central

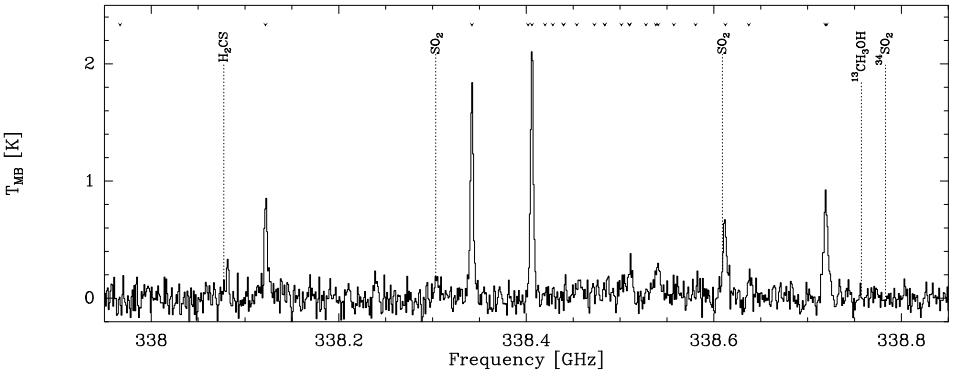

Figure 4.34: *S255:* Spectrum of the maser position. The tick marks at the top indicate the frequencies of the methanol lines.

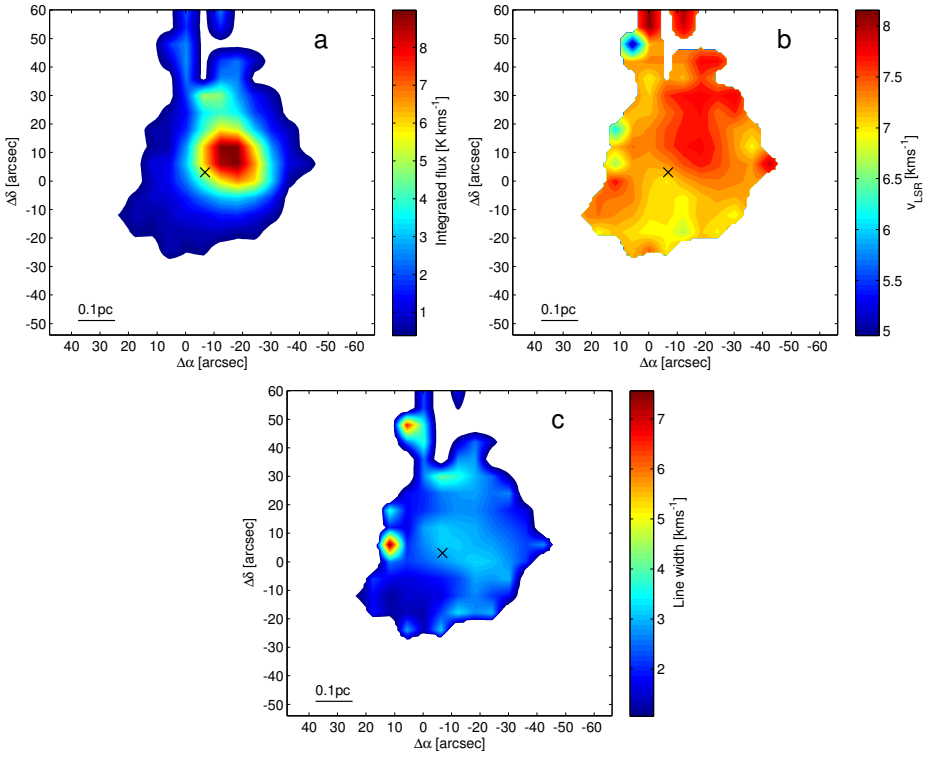

Figure 4.35: As Fig. 4.2 for the source S255.

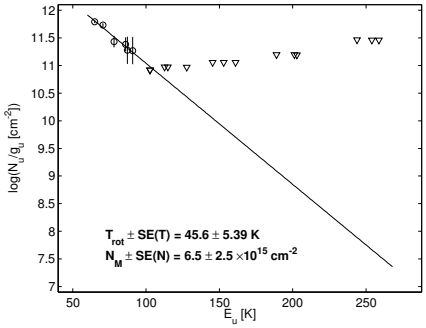

Figure 4.36: *S255:* Rotation diagrams for the positions of the maser.

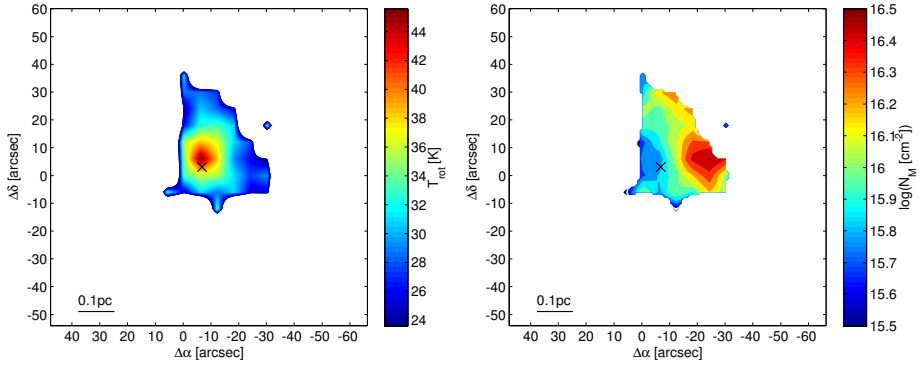

Figure 4.37: *S255:* Maps of CH_3OH rotation temperature and column density.

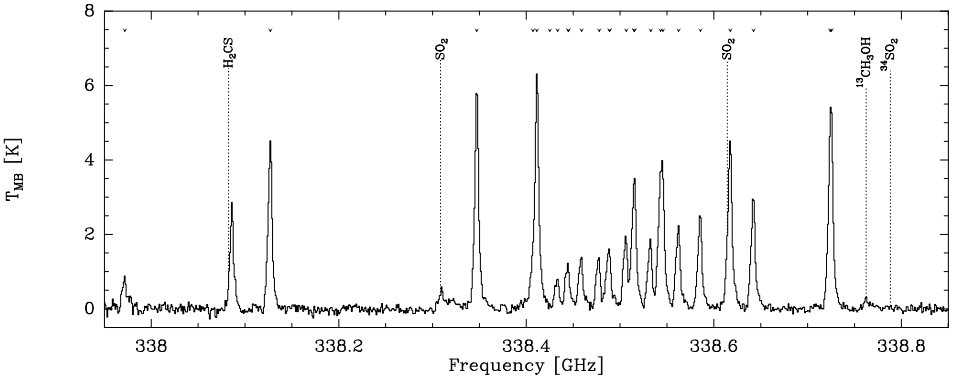

Figure 4.38: *W3(OH):* Spectrum at the maser positions. The tick marks at the top indicate the frequencies of the methanol lines.

source S255IR has a luminosity of 2.4×10^4 $L_\odot$, and higher-resolution mm continuum observations have revealed that it breaks up into three separate mm cores: SMA1, SMA2, SMA3. There are several outflows that interact in the region, but the outflow originating from S255IR-SMA1 (associated with the methanol masers) is oriented roughly NE (red) - SW (blue) (Wang et al. 2011).

The −1E line maps of S255 (Figs. 4.35) show that emission is roughly circular and shows a maximum in the central region of the map, to the NW of the position of the methanol maser ($\Delta\alpha$=-6.8″, $\Delta\delta$=+3.0″). The velocity map is complex, but there seems to be a velocity gradient across the maser position with redshifted emission associated with the line flux peak to the NW and more blueshifted emission to the S. The line width map is also complex but it appears that the line width is larger to the NW of the maser than to the S of the maser. Some interference in receptor R15 was seen in the data reduction process and consequently it was masked out.

The spectrum of the maser region (Fig. 4.34) shows that lines up to K=2 are detected. The v_t = 1 line is not detected and the SO_2 emission does not contribute significantly to the +1E line which is included in the rotation diagram analysis (Fig. 4.36). The rotation temperature has a maximum close to the position of the maser, to the E of the CH_3OH −1E line flux maximum (Fig. 4.37). The column density map indicates that the higher column densities are associated with the redshifted emission to the NW of the maser position and lower column densities with the blueshifted emission to the S.

4.3.12 W3(OH)

The well known UCHII region W3(OH) with a parallax distance estimate of 1.95 kpc (Xu et al. 2006) is part of the extensively studied W3 complex that houses many different stages of star formation (Helmich & van Dishoeck 1997). The 6.7 GHz CH_3OH maser emission is associated with the UCHII region (Harvey-Smith & Cohen 2006). Six

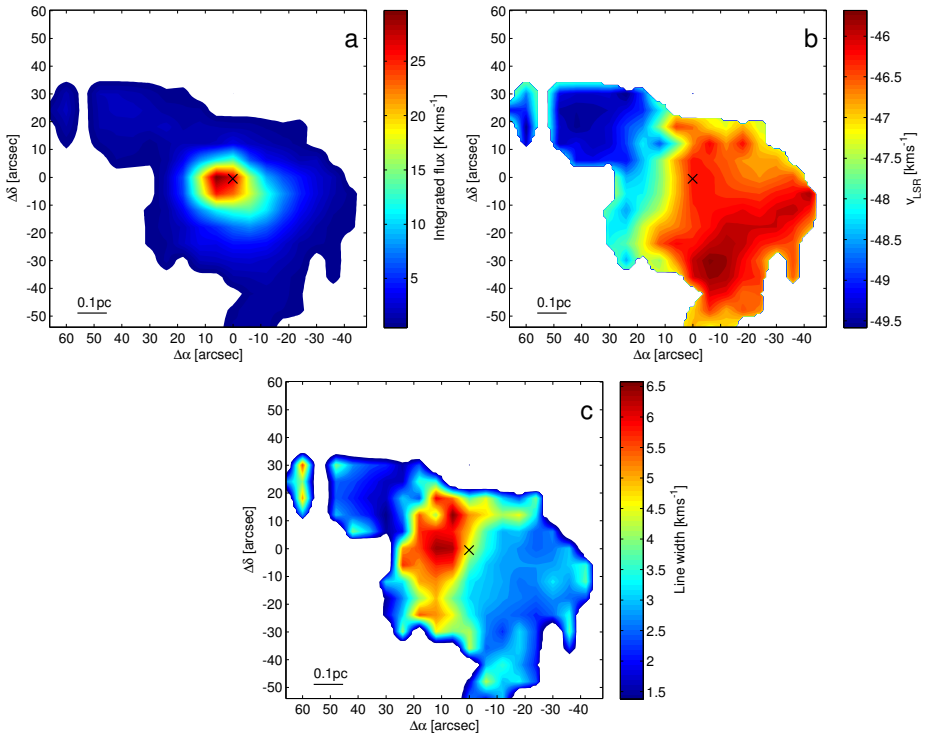

Figure 4.39: As Fig. 4.2 for the source W3(OH).

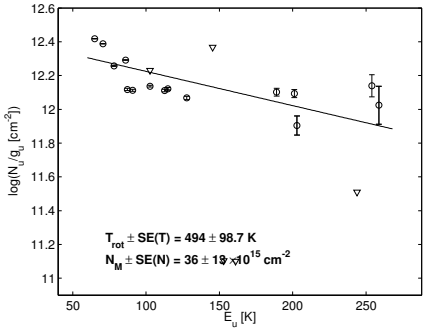

Figure 4.40: *W3(OH):* Rotation diagram of CH_3OH for the position of the maser.

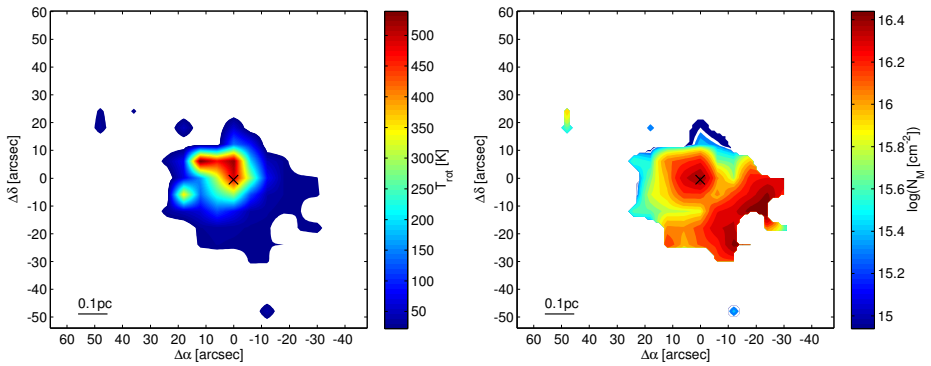

Figure 4.41: *W3(OH):* Maps of CH_3OH rotation temperature and column density.

arc seconds to the East of W3(OH) is the hot core W3(H_2O) (van der Tak et al. 2000b, Bisschop et al. 2007). W3(OH) has a luminosity of 8×10^4 $L_\odot$ and W3(H_2O) has a luminosity of 2.4×10^4 $L_\odot$. In W3(OH) the mm-continuum emission is dominated by free-free emission, whereas in W3(H_2O) it is dominated by dust emission (Stecklum et al. 2002). High-resolution interferometric observations have confirmed the chemical differentiation of the two sources where O-bearing species such as CH_3OH are present in both sources whereas N-bearing species only are present in W3(H_2O) (Wyrowski et al. 1999).

The −1E line maps of W3(OH) (Fig. 4.39) show that the CH_3OH emission has higher line fluxes towards the centre of the map close to the position of the methanol maser ($\Delta\alpha$=+0.1″, $\Delta\delta$=-0.5″). The velocity map shows a large scale velocity gradient with redshifted velocities in the SW and blueshifted velocities towards the NE. The line width map shows that the large line widths are associated with the blueshifted emission to the NE of the maser and that the redshifted emission to the SW is associated with smaller line widths.

The spectrum of the maser region shows that lines up to K=5 are detected and line wings are seen in the lines. Notably the $v_t = 1$ at 337.97 GHz is clearly detected and shows a complex line structure. There is a small amount of SO_2 but we have deemed its contribution small enough that we include the +1E line in the rotation diagram analysis. There may be a second gas component (offset in velocity) seen in the CH_3OH emission but the complexity of the spectrum and line blending prohibits us from separating the two components. Furthermore, because of the $^{13}CH_3OH$ detection, optical depth effects cannot be neglected (Fig. 4.40) and it is clear that the rotation diagram analysis breaks down in the centre region.

The rotation temperature map of W3(OH) (Fig. 4.41) shows a maximum at the position of the maser and extending to the NE, towards the more blueshifted emission. The column density map shows a maximum at the position of the maser and also an enhancement to the SW associated with the redshifted emission.

Table 4.3: Derived rotation temperatures and methanol column densities at the position of the maser.

Source	$\Delta\alpha$ ($''$)	$\Delta\delta$ ($''$)	$T_{\rm rot}$ (K)	$N_{\rm M}$ (cm^{-2})
AFGL5142	+30.1	+2.6	65.2 ± 12.0	$1.1 \pm 0.7 \times 10^{16}$
DR21 FIR1	-0.3	+0.1	24.1 ± 4.3	$1.5 \pm 1.2 \times 10^{16}$
DR21 FIR2	+17.6	+22.3	39.5 ± 6.0	$4.3 \pm 2.3 \times 10^{15}$
G23.207−00.377	+0.2	-3.9	51.1 ± 4.2	$2.0 \pm 0.5 \times 10^{16}$
G23.389+00.185	-0.1	-0.1	67.0 ± 18.3	$6.6 \pm 5.1 \times 10^{14}$
G23.657−00.127	–	–	158.6 ± 78.1	$8.3 \pm 8.4 \times 10^{14}$
G24.541+00.312	–	–	–	–
G40.62−0.14	+0.1	+0.1	92.5 ± 26.3	$9.7 \pm 6.9 \times 10^{14}$
G73.06+1.80	+0.6	+0.7	50.5 ± 10.0	$1.3 \pm 0.8 \times 10^{15}$
G78.12+3.63	-0.6	+1.7	222.3 ± 89.6	$4.4 \pm 3.6 \times 10^{15}$
L1206	-4.3	-1.7	2342.6 ± 4456.0	$1.6 \pm 4.7 \times 10^{16}$
S255	-6.8	+3.0	45.6 ± 5.4	$6.5 \pm 2.5 \times 10^{15}$
W3(OH)	+0.1	-0.5	493.6 ± 98.7	$3.6 \pm 1.3 \times 10^{16}$

Notes: The maser position is given in $\Delta\alpha$ and $\Delta\delta$ relative to the map centre. The two sources G23.657−00.127 and G24.541+00.312 were observed in single pointing mode and therefore do not have any offsets. Too few lines were detected in G24.541+00.312 to perform a rotation diagram analysis.

4.4 Analysis

4.4.1 Rotation diagram analysis

The results of our rotation diagram analysis are summarised in Table 4.3 which lists the derived rotation temperatures and column densities for the positions of the methanol masers. We find typical rotation temperatures between 25 and 100 K and column densities between 6×10^{14} and 2×10^{16} cm^{-2}. For sources which have a simple structure both the rotation temperature peak and column density peak is closely associated with the maser position (< 0.1 pc). This result is similar to what we found in Chapter 3. However, in Cep A HW2 we were able to identify two different velocity components at the maser position with the second component presumably associated with the maser emission. A more detailed analysis of the second gas component, using population diagram and non-LTE modelling, revealed that in fact the column density was significantly higher for this gas component but that beam dilution and optical depth effects made the rotation diagram analysis break down (Chapter 3).

4.4.2 CH_3OH gas distribution

To compare the CH_3OH gas distribution of the sources in our sample we have fitted a two dimensional Gaussian to the integrated flux of the −1E line. The emission is represented by an ellipse with corresponding offset from the map centre, major/minor axis, and position angle. To determine the linear scales the distances in Table 4.1 were used. The results of the fits are presented in Table 4.4. For sources that we mapped we have determined the distance r between the methanol maser position and the centre of the ellipse. It should be noted that although the beam size of the JCMT at 338 GHz is 14″, the signal-to-noise ratio of our data allows us to determine the positions and source sizes to a fraction of the beam width. Moreover, the velocity field in the −1E maps indicates that the sources are resolved.

Based on the morphology of the −1E line maps we have divided the sources into three separate classes: weak (*W*), compact (*C*), and extended (*E*). The two weak sources G23.657−00.127 and G24.541+00.312, for which the distance estimate of G23.657−00.127 is based on parallax measurements, are amongst the more distant sources in our sample. Because the sources were observed in a single deep pointing we cannot map these sources and therefore we have no reliable size estimates.

In the seven compact sources of our sample, the CH_3OH −1E line emission is isolated and confined to a well defined region of the maps with the peak of the −1E line flux close to the maser position ($r < 0.05$ pc). Furthermore, the velocity maps indicate a relatively simple velocity field. The distances to the seven sources span from 0.78 kpc to 4.6 kpc, though only for L1206 and G78.12 are the distance estimates based on parallax measurements. Nevertheless, the compact sources have major axes between 10″ and 20″ which correspond to physical sizes between ∼0.04 pc and ∼0.4 pc. As discussed in Sec. 4.3 most of these sources have been observed in other molecules. With the exception of G23.207−00.377 all compact sources can be fitted with a simple linear velocity gradient along the major axes. The fitted linear velocities $v_{\rm lin}$ are between −1.4 and 12.4 km s^{-1} pc^{-1} (Table 4.4, column 10). A similar physical extent and velocity gradient is seen in Cep A, where the gas is part of the HW2 wide-angle outflow. So including Cep A, we have a sample of 14 sources, of which eight sources are C-type.

The three extended sources in our sample DR21, S255, and W3(OH) all have measured parallaxes with corresponding distances between 1.45 and 2.0 kpc. In these three sources, the CH_3OH −1E line emission is extended over 0.3 − 0.5 pc and shows a complex velocity field in the central velocity maps. Fitting 2D Gaussians is not appropriate for these sources, which are part of larger-scale molecular cloud complexes, and have already been extensively discussed in the literature.

Table 4.4: Results of the 2D Gaussian fit of the integrated −1E line emission.

Source	Class	$\Delta\alpha$ ($''$)	$\Delta\delta$ ($''$)	a ($''$)	b ($''$)	PA (°)	a (pc)	b (pc)	$v_{\rm lin}$ (km s^{-1} pc^{-1})	r (pc)	σ_r (pc)
AFGL5142	*C*	+33.00	+3.48	20.0	15.8	5.7	0.17	0.14	6.78	0.027	0.009
DR21 FIR1	*E*	+19.53	+40.48	67.0	19.1	26.8	0.47	0.13	–	0.316	0.007
DR21 FIR2	*E*	+19.53	+40.48	67.0	19.1	26.8	0.47	0.13	–	0.129	0.007
G23.207−00.377	*C*	-1.62	-3.00	15.8	12.2	72.7	0.355	0.273	–	0.045	0.022
G23.389+00.185	*C*	+0.54	+1.08	10.3	9.6	-74.0	0.223	0.208	-1.37	0.028	0.022
G23.657−00.127	*W*	–	–	–	–	–	–	–	–	–	0.016
G24.541+00.312	*W*	–	–	–	–	–	–	–	–	–	0.028
G40.62−0.14	*C*	-1.06	-1.55	11.1	10.1	-58.4	0.12	0.11	6.03	0.021	0.011
G73.06+1.80	*C*	+0.13	-0.15	11.6	9.7	79.5	0.28	0.23	1.7	0.021	0.024
G78.12+3.63	*C*	-2.42	+3.70	14.3	9.6	-51.2	0.12	0.08	12.4	0.023	0.008
L1206	*C*	-3.30	+1.56	10.9	8.2	2.5	0.041	0.031	7.44	0.013	0.004
S255	*E*	-12.30	+12.72	34.5	22.2	4.4	0.27	0.17	–	0.086	0.008
W3(OH)	*E*	+1.08	-5.09	38.5	22.9	56.0	0.36	0.22	–	0.044	0.010

Notes: The in offsets in RA ($\Delta\alpha$) and DEC ($\Delta\delta$) are measured from the map centre, also reported are the major axes (a), minor axes (b), and position angles (PA). The linear scales are based on the distances in Table 4.1. $v_{\rm LIN}$ is the linear velocity gradient measured along the major axis and r is the maser offset from the centre of the fitted 2D Gaussian. The two sources G23.657−00.127 and G24.541+00.312 were observed in single pointing mode and are only included in the table for completeness.

4.4.3 Population diagram analysis

The environment close to the protostar is expected to be quite different from the more extended emission region. In particular, the excitation of the methanol maser requires specific conditions and the maser extent is typically only a few hundred to a couple of thousand AU, see Chapter 5 (e.g. Bartkiewicz et al. 2009). Therefore, to investigate the influence of source size/clumpiness and optical depth effects on our data we have performed a population diagram (PD) analysis of the spectra at the maser position. The analysis is performed as a χ^2 test in which the methanol column density, excitation temperature, source size, are varied to minimise the χ^2 difference between the synthetic and observed spectra. In the process the optical depths of the transitions are also calculated. The beam filling factor $f = \Omega_s/\Omega_a$ is assumed to be the same for all lines, although in reality the highly excited lines could have a smaller extent than the lines with lower excitation temperatures. In the two extreme cases that all lines are optically thick and all lines are optically thin the method is degenerate in $f \times T_{ex} = Constant$ and $f \times N_M = Constant$, respectively. However, this degeneracy is broken if both optically thin and optically thick lines are observed. For a detailed discussion on the PD analysis see Goldsmith & Langer (1999) and Wang et al. (2010). In order for the method to work a minimum of three lines need to be observed, therefore we have only performed this analysis in the centre region where more lines are detected. For each best fit we can check the optical depth of all lines.

We have used column densities from 10^{14} to 10^{18} cm^{-2}, excitation temperatures from 10 to 500 K and beam filling factors between 0.01 and 1 (corresponding to source sizes between 1.5″ and > 14″. The results of the analysis for the individual sources are summarised in Table 4.5. We do not find any large beam dilution effects in our analysis, nor very high optical depths. Compared to Cep A the apparent lack of small source sizes may be because for most sources only the low−K lines have integrated fluxes larger than our signal-to-noise cut-off ratio of six. The main contribution to the low-K line emission likely comes from the more extended gas rather than the gas directly associated with the maser region, as in Cep A (Chapter 3). In fact, for several sources we find lower excitation temperatures than what was found in the rotation diagram analysis. This results from the fact that we infer moderate optical depths ($\tau \approx 1$) for the lower K lines. The optical depth correction raises the population estimates of those levels, thus lowering the derived excitation temperature. We find beam-averaged column densities between 3×10^{14} and 10^{16} cm^{-2}. Taking the beam filling factor into account the corrected total column densities are a few times higher (4×10^{14} to 4×10^{16} cm^{-2}). These column densities are similar to what we found for the methanol gas associated with the larger scale outflow at the maser position in Cep A. For the second gas component in Cep A, presumed to be associated with the maser emission, we found a column density of a few times 10^{17} cm^{-2}, at least an order of magnitude higher than found here. Furthermore, in the sources where the $v_t = 1$ line is detected, it seems to have a small offset in velocity compared to the low-K lines of the $v_t = 0$ band. All these reasons suggest that we are primarily probing the more extended CH_3OH gas, and to a much lesser extent the highly excited masing gas.

Table 4.5: Results of the population diagram analysis.

Source	$\Delta\alpha$ ($''$)	$\Delta\delta$ ($''$)	$T_{\rm ex}$ (K)	$N_{\rm M}$ (cm^{-2})	Ω_s/Ω_a	$\tau_{\rm min}$	$\tau_{\rm max}$
AFGL 5142	30.1	0.0	20.8	7.4×10^{15}	1	0.002	1.16
DR21 FIR1	-3.2	-0.08	12.9	1.9×10^{15}	1	0.036	0.19
DR21 FIR2	14.7	23.3	12.9	4.0×10^{15}	0.91	0.02	0.40
G23.207−00.377	3.0	-2.6	20.8	1.0×10^{16}	1	0.13	1.57
G23.389+00.185	0.0	0.0	20.8	4.0×10^{14}	0.81	0.0052	0.063
G23.657−00.127	0.0	0.0	48.5	2.9×10^{14}	0.76	0.0079	0.026
G24.541+00.312							
G40.62−0.14	0.3	2.9	24.8	5.4×10^{14}	0.81	0.0055	0.085
G73.06+1.80	0.1	0.3	16.8	6.3×10^{15}	0.16	0.18	0.90
G78.12+3.63	-3.2	3.0	28.7	1.6×10^{15}	0.91	0.0010	0.23
L1206	-3.0	-2.8	340	1.4×10^{15}	0.76	0.0008	0.0025
S255	-6.3	6.0	16.8	3.4×10^{15}	0.95	0.096	0.48
W3	-2.6	0.1	99.2	5.8×10^{15}	0.95	0.0059	0.16

4.5 Discussion

We have mapped the large scale ($10''-50''$) distribution of the CH_3OH $J = 7_K \rightarrow 6_K$, v_t=0, band towards 14 regions (including Cep A) of high-mass star formation associated with 6.7 GHz methanol masers. Two sources are too weak (W) to map and will be partly excluded from this discussion. The eight compact (C) sources are characterised by the CH_3OH emission being confined to a < 0.4 pc region and with a single peak close to the maser position in the integrated flux maps. In the remaining three sources, the emission is extended (E) over $0.3 - 0.5$ pc without a clear peak in the maps of the line flux, velocity, and line width.

The largest uncertainty in our analysis stems from the poor distance estimate of half of our sample. Only for seven sources are the distance estimates based on parallax measurements (Cep A and L1206 are the only compact sources with measured parallax), typically accurate to within ∼10%. For the remaining sources in the sample the distance estimate is found in the literature and based on the kinematic distance, accurate to a factor of ∼2.

4.5.1 Excitation of CH_3OH gas

To characterise the large scale physical conditions of the gas we have performed a pixel-based rotation diagram analysis for the sources for which we have a sufficiently high signal to noise ratio. We typically find the highest rotation temperatures close to the maser position. The column density peak seems to be less closely associated with the maser position. Note that this is similar to what we found in Cep A initially, where closer inspection of the excitation on smaller scales proved that the highest column densities

occur at the maser position. Typical rotation temperatures for the large scale distribution are 30 to 50 K and column densities between 10^{15} and 10^{17} cm^{-2}, similar to what we found in Cep A (Chapter 3).

Because the 6.7 GHz CH_3OH maser is typically located within $\sim$ 1000 AU of the protostar(s) responsible for the excitation of the masing gas (Bartkiewicz et al. 2009), we therefore expect the highly excited gas to have a similar small extent. To investigate optical depth and beam dilution effects a population diagram analysis was performed on the gas at the maser positions. However, we do not see the need for large beam dilution effects in our analysis. One possible explanation for this is that we mainly detect the lower K lines and that the main contribution to the emission of these lines comes from the more extended gas. In Cep A we were able to distinguish two different gas components, one component with strong low-K lines associated with the large scale structure, and a second component associated with the masing gas and much more readily detected in the high-K lines. In the thermal CH_3OH spectra of the sources in our sample we are not able to identify more than one single gas component and at most positions the line shape appears Gaussian. A possible explanation may be the relatively large distances of the sources in our sample (with the exception of L1206) compared to that of Cep A (700 pc, see below).

In fact, in the population diagram analysis we find for several sources a lower excitation temperature than we find in the rotation diagram analysis. For these sources we also find that the optical depth of the lowest K lines is not negligible ($\tau \approx 1$). The optical depth correction and consequently lower excitation temperature in the population diagram analysis also leads to somewhat lower estimates of the column density. The general lack of detection of the $^{13}CH_3OH$ ($13_{0,13} \rightarrow 12_{1,12}$) A^+ $v_t = 0$ line with an upper energy level of 206 K and high transition probability ($S\mu^2 = 1.11$), indicates that the optical depth is at most moderate.

An independent indication of highly excited CH_3OH gas is the detection of the -1A $v_t = 1$ line at 337.97 GHz in approximately half of the sources in our sample. Because collisional pumping alone is very inefficient at populating the torsionally excited state, the $v_t = 1$ line is an indicator of infrared pumping at work (Leurini et al. 2007). The sources for which the $v_t = 1$ line is detected also show signs of the high-K lines, supporting the argument of highly excited gas. Although high-K lines are weak, we have a considerable detection rate of the $v_t = 1$ line. The high detection rate of the $v_t = 1$ line could be an effect of our sample selection, because we have intentionally targeted bright 6.7 GHz methanol maser sites, which are thought to be pumped by infrared radiation. For both the $v_t = 1$ line and the high-K lines beam dilution effects are likely important. There does however not seem to be any correlation between the distance of the source or the luminosity and the occurrence of the $v_t = 1$ line which one might expect. Neither are the sources with the $v_t = 1$ line detection those with the largest integrated flux of the -1E line. Instead, the $v_t = 1$ line seems to be correlated with the sources for which we find a non-negligible optical depth in the low-K lines in the population diagram analysis. Higher resolution interferometric observations with beam sizes similar to the extent of the maser regions (and more accurate distance estimates) would greatly help to constrain the excitation of the highly excited gas (Beuther et al. 2007c).

4.5.2 Morphology

The three extended sources all have accurate distance estimates and are excellent candidates for detailed studies, however the complexity of the sources makes them less suitable for the analysis method applied here. Therefore, the remainder of the discussion will focus on the eight sources classified as compact.

The CH_3OH $-1E$ emission of the compact sources is confined to a central peak in the integrated $-1E$ flux maps. The confined emission and central peak indicates that, as in Cep A, there is a single source of CH_3OH production in these sources. We have characterised the $-1E$ line emission by a 2D Gaussian and find it centred close to the maser positions ($r < 3.4''$). The absolute pointing accuracy of the observations is $\sim 1''$ which means that the maser may be somewhat offset from the peak of the $-1E$ line flux, similar to what has been seen in Cep A. All but one of the compact sources (G23.207−00.377) show a simple linear velocity gradient along the major axis, further strengthening the argument for a central origin of the CH_3OH gas. We suggest that the velocity field indicates a young, large opening angle outflow, similar to what is found in Cep A (Chapter 3).

Although the source sizes that we find are similar to the beam of the JCMT telescope in several cases, the signal-to-noise ratio of the data allows us to measure the position and size of the sources to a few arc seconds accuracy, and we therefore argue that the sources are resolved. This argument is further supported by the velocity gradients seen in the central velocity maps (and along the major axes). Using the adopted distances in Table 4.1 we find major axes between 0.04 and 0.4 pc. The chemical life-time of CH_3OH is expected to be a few 10^4 years (van der Tak et al. 2000a). Assuming a common age of 2.4×10^4 (as found in Cep A) we find expansion velocities of 0.8 to 8 km s^{-1}(similar to the 5.8km s^{-1} we find in Cep A). The spread in expansion velocities could have at least three origins. First of all, the sources may not have the same age. Secondly, it could be an orientation effect. Outflows in the plane of the sky have larger apparent extent than outflows oriented towards/away from us. The fitted linear velocity gradient along the major axes tends to be higher for the sources with smaller extents, supporting the argument of orientation effects playing a role. Thirdly, the linear velocity gradient depends directly on the distance, and the uncertainties of the distance estimates are substantial for all the compact sources but Cep A and L1206.

Finally, we also note that the H_2CS feature at ∼338.08 GHz appears to be common towards regions of star formation (e.g. van der Tak et al. 2003). In most sources in our sample the H_2CS seem to be offset by a few km s^{-1} from the CH_3OH , implying that it may trace another gas component.

4.6 Conclusions

We have performed JCMT observations of the thermal CH_3OH gas in a sample of 12 high-mass star forming regions. Thermal CH_3OH ($J = 7_K \rightarrow 6_K$) emission was detected towards all sources although for two of the sources the emission was not bright enough to be mapped. The rotation diagram analysis method was used to analyse the large scale

excitation of the gas and towards the maser positions where more lines were detected we have performed a population diagram analysis. The main conclusions of this work are:

- In most sources the thermal CH_3OH emission is confined and shows a single peak close to the maser position in the integrated flux maps, consistent with a single source of origin of the CH_3OH gas.
- A large fraction of sources show a linear velocity gradient along the major axis of the integrated flux of the -1E line, indicating an outflow, probably young and with a large opening angle.
- In the population diagram analysis we find no evidence of a small highly excited gas component as characteristic of hot cores. However this may be because we are not able to separate the highly excited gas in the core from the more extended thermal CH_3OH emission.
- The population diagram analysis indicates that in half of the sources the optical depth of the low-K lines is not negligible which results in somewhat lower estimates of the excitation temperature and column density than what we find in the rotation diagram analysis.
- There is evidence of the CH_3OH $J = 7 \rightarrow 6$ A^+ $v_t = 1$ line in half of the sources. The detection of this line may indicate radiative pumping and the high detection rate is probably due to the source selection. The $v_t = 1$ line and the high-K lines could come from a region of ~ 1000 AU, seriously affected by beam dilution at the current resolution.
- Half of the sources in our sample have measured parallaxes. For the remaining sources, with kinematic distance estimates, the major uncertainty in our analysis is the accuracy of the distance estimate.
- Assuming radiative excitation is important on 1000 AU scales, with the onset of ALMA, high-resolution imaging of thermal CH_3OH emission is possible for large source samples. This will shed light on the origin of the CH_3OH masers.

Acknowledgements

This research was supported by the EU Framework 6 Marie Curie Early Stage Training programme under contract number MEST-CT-2005-19669 “ESTRELA”.